

# *Ab initio* analysis of the tight-binding parameters and magnetic interactions in $\text{Na}_2\text{IrO}_3$

Kateryna Foyevtsova,<sup>1</sup> Harald O. Jeschke,<sup>1</sup> I. I. Mazin,<sup>2</sup> D. I. Khomskii,<sup>3</sup> and Roser Valentí<sup>1</sup>

<sup>1</sup>*Institut für Theoretische Physik, Goethe-Universität Frankfurt, 60438 Frankfurt am Main, Germany*

<sup>2</sup>*Code 6393, Naval Research Laboratory, Washington, DC 20375, USA*

<sup>3</sup>*II. Physikalisches Institut, Universität zu Köln, Zùlpicher Strasse 77, 50937 Köln, Germany*

(Dated: January 18, 2018)

By means of density functional theory (DFT) calculations (with and without inclusion of spin-orbit (SO) coupling) we present a detailed study of the electronic structure and corresponding microscopic Hamiltonian parameters of  $\text{Na}_2\text{IrO}_3$ . In particular, we address the following aspects: (i) We investigate the role of the various structural distortions and show that the electronic structure of  $\text{Na}_2\text{IrO}_3$  is exceptionally sensitive to structural details. (ii) We discuss both limiting descriptions for  $\text{Na}_2\text{IrO}_3$ ; quasi-molecular orbitals (small SO limit, itinerant) versus relativistic orbitals (large SO limit, localized) and show that the description of  $\text{Na}_2\text{IrO}_3$  lies in an intermediate regime. (iii) We investigate whether the nearest neighbor Kitaev-Heisenberg model is sufficient to describe the electronic structure and magnetism in  $\text{Na}_2\text{IrO}_3$ . In particular, we verify the recent suggestion of an antiferromagnetic Kitaev interaction and show that it is not consistent with actual or even plausible electronic parameters. Finally, (iv) we discuss correlation effects in  $\text{Na}_2\text{IrO}_3$ . We conclude that while the Kitaev-Heisenberg Hamiltonian is the most general expression of the quadratic spin-spin interaction in the presence of spin-orbit coupling (neglecting single-site anisotropy), the itinerant character of the electrons in  $\text{Na}_2\text{IrO}_3$  makes other terms beyond this model (including, but not limited to 2nd and 3rd neighbor interactions) essential.

PACS numbers: 75.10.-b, 75.10.Jm, 71.70.Ej, 71.15.Mb

## I. INTRODUCTION

The electronic and magnetic behavior of layered 5d transition metal oxides<sup>1</sup> has been a subject of intensive discussion in the last years. Particularly exciting has been the suggestion by the authors of Ref. 2 that hexagonal iridates such as  $\text{Na}_2\text{IrO}_3$  are a realization of the nearest neighbor Kitaev-Heisenberg (nnKH) model:

$$H_{ij}^{(\gamma)} = 2KS_i^\gamma S_j^\gamma + JS_i \cdot S_j \quad (1)$$

This proposal is based on the premise that spin-orbit (SO) coupling is the most important energy scale for the description of these systems so that Ir 5d  $t_{2g}$  orbitals are written in terms of  $j_{\text{eff}} = 1/2$  and  $j_{\text{eff}} = 3/2$  relativistic orbitals, with the Kramers doublet  $j_{\text{eff}} = 1/2$  represented by the operator  $S = 1/2$ . The combination of Kitaev and Heisenberg terms leads to a complex phase diagram with various magnetic and spin-liquid phases<sup>2-4</sup>. Obviously, some of these properties can only manifest themselves when the Kitaev term dominates or is at least comparable to the Heisenberg term. Also, other possible contributions, such as magnetic anisotropy, ring exchange or biquadratic exchange, to mention a few, may alter the phase diagram and the properties of the model considerably. Most importantly, while the Kitaev-Heisenberg expression is the most general fully-symmetric expression for anisotropic pairwise magnetic interactions in the second order in spin in the presence of SO coupling (just as the Heisenberg exchange represents the same in the isotropic non-relativistic case), it is not necessarily short ranged in the presence of considerable itinerancy.

So far, essentially all analyses of the nnKH model for  $\text{Na}_2\text{IrO}_3$  have been performed in the localized limit, where an assembly of weakly interacting relativistic atomic orbitals is assumed to be a good starting approximation. On the other hand, first principles calculations suggest considerable delocalization of electrons over individual Ir hexagons building quasi-molecular orbitals (QMOs)<sup>5</sup>. The associated “itinerant” energy scale (the band width) is  $\approx 1.5$  eV, to be compared to the single-site spin-orbit splitting scale<sup>6</sup>  $(3/2)\lambda \approx 0.7$  eV and the Hubbard and Hund’s rule correlation energy scale of  $U - J_H \approx 0.5 - 1$  eV. This makes the entire premise of the nnKH model questionable. At the same time, it has also been pointed out<sup>7,8</sup> that the nnKH model with the addition of the 2nd and 3rd neighbors Heisenberg interaction is easier to reconcile with the experimental data. Such relatively long-range exchange interaction is another hallmark of considerable itinerancy (here and below, when we speak of itinerancy, we imply mostly delocalization over Ir<sub>6</sub> rings, but not necessarily over the entire crystal).

In the present work we revisit and discuss the validity of both limiting descriptions for  $\text{Na}_2\text{IrO}_3$ ; itinerant (QMO picture) versus localized ( $j_{\text{eff}} = 1/2$  Kramers doublet). To this end, we perform a thorough analysis of the electronic properties of  $\text{Na}_2\text{IrO}_3$  within *non-relativistic* and *relativistic* density functional theory (DFT) and derive, using projection on Wannier functions, the relevant hopping parameters and show that QMOs are naturally obtained as linear combinations of Ir  $t_{2g}$  Wannier functions. We discuss the relation between the quasi-molecular orbital and the relativistic orbital,  $j_{\text{eff}}$ , representations and show that the behavior of  $\text{Na}_2\text{IrO}_3$  lies in

between a fully localized and fully itinerant description. Finally, the parametrization of the electronic bandstructure allows us to provide realistic estimates for the model parameters in the localized nnKH model. We thus investigate whether we are close to a regime where the Kitaev interaction plays a decisive role or not.

Quite unexpectedly, we find that  $\text{Na}_2\text{IrO}_3$  is an example of a material where minor details of the crystal structure can dramatically affect the electronic structure, and simple guessing of the band structure parameters, or estimating them from simplified crystallographic models (so far all model calculations for this compound were utilizing one or the other approach) can be exceptionally misleading. In fact some of the models energetically discussed in the community, while of undeniable theoretical appeal, are not even qualitatively close to the actual parameter range in  $\text{Na}_2\text{IrO}_3$ .

While this particular compound is very intriguing and has been enjoying extraordinary popularity lately, we want to emphasize that this strong dependence of the electronic properties on details of the crystal structure is an important result, whose relevance goes beyond specifically  $\text{Na}_2\text{IrO}_3$  and is likely true for many other materials based on honeycomb transition-metal layers.

The paper is organized as follows. In Section II we review the crystal structure and magnetic properties of  $\text{Na}_2\text{IrO}_3$ . In Section III we provide details of the DFT calculations and the projector method. In Section IV we present the results of the electronic structure analysis without inclusion of spin-orbit coupling and analyze the role of the structural distortions in  $\text{Na}_2\text{IrO}_3$ . In Section V we investigate the role of spin-orbit coupling and discuss the relation between the QMOs and the relativistic orbitals ( $j_{\text{eff}}$ ). In this context, we discuss whether the existing experimental situation can distinguish between the DFT description (with the resulting itinerancy) and localized ( $j_{\text{eff}} = 1/2$ ) models. We proceed with an analysis of the single-site magnetic anisotropy in  $\text{Na}_2\text{IrO}_3$  and find it to be relevant (pure  $j_{\text{eff}} = 1/2$  states do not have any single-site anisotropy). In Section VI we provide *ab initio*-derived estimates for the parameters appearing in the Kitaev and Heisenberg terms in  $\text{Na}_2\text{IrO}_3$  and discuss the validity of the nnKH model by considering the experimentally observed magnetic order and attempts to explain it from a local point of view. Finally in Section VII we present our conclusions.

## II. CRYSTAL STRUCTURE AND MAGNETIC PROPERTIES OF $\text{Na}_2\text{IrO}_3$

$\text{Na}_2\text{IrO}_3$  crystallizes in the monoclinic space group  $C2/m$  (No. 12)<sup>8</sup> (see Fig. 1) and consists of Ir honeycomb layers (Fig. 1 (b)) stacked along the monoclinic  $c$  axis (Fig. 1 (a)) with an in-plane off-set along  $a$ . Na ions occupy both the interlayer positions and 1/3 of the in-plane positions at the centers of Ir hexagons. This structure can be visualized as proceeding from  $\text{NaIrO}_2$

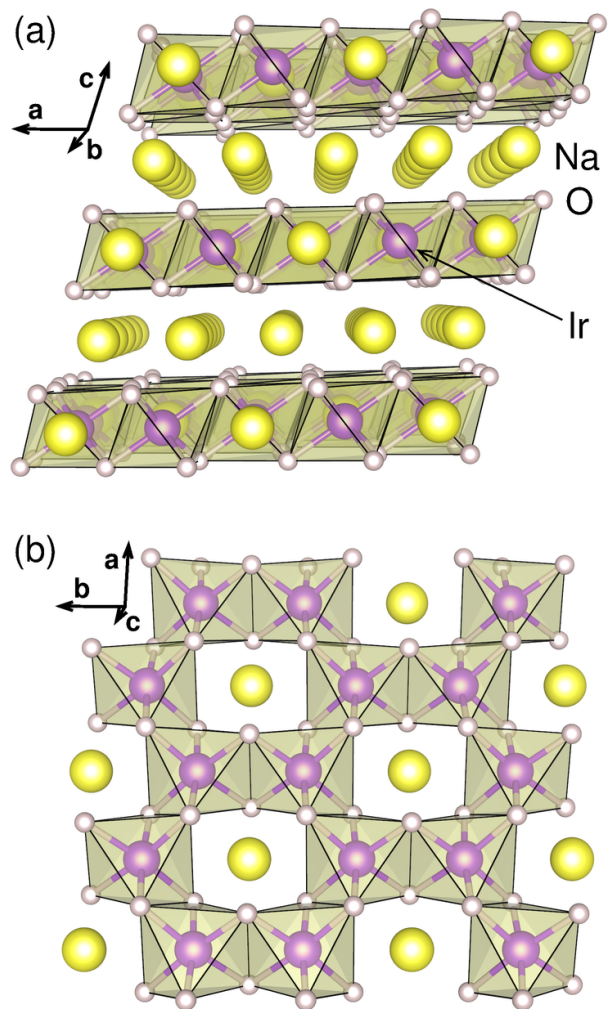


FIG. 1: Crystal structure of  $\text{Na}_2\text{IrO}_3$ . (a) Projection on the  $ac$  plane and (b) projection on the  $ab$  plane.

with a  $\text{CdI}_2$  structure with triangular  $\text{IrO}_2$  layers. In these layers 1/3 of the in-plane iridium atoms are substituted by extra Na, *i. e.*, its formula can be written as  $\text{Na}(\text{Na}_{1/3}\text{Ir}_{2/3})\text{O}_2$ , which, multiplied by 3/2, gives the usual formula of  $\text{Na}_2\text{IrO}_3$ <sup>9</sup>.

An idealized crystal structure of this kind corresponds to having all nearest neighbor (NN) Ir-Ir and NN Ir-O distances equal and Ir-O-Ir angles of 90 degrees. The experimental structure of  $\text{Na}_2\text{IrO}_3$  departs from the idealized case and shows a few distortions: (i) orthorhombic distortion that introduces inequality among NN Ir-Ir distances and among NN Ir-O distances, (ii)  $\text{IrO}_6$  octahedra rotations that place O atoms on the faces of a cube containing an Ir hexagon (see Fig. 2 of Ref. 5) and (iii) trigonal distortion which is a compression of the  $\text{IrO}_6$  octahedra in the  $c$ -direction that induces a departure from 90 degrees of the Ir-O-Ir angles. In Section IV we will discuss the effect of these distortions on the electronic structure of  $\text{Na}_2\text{IrO}_3$ .

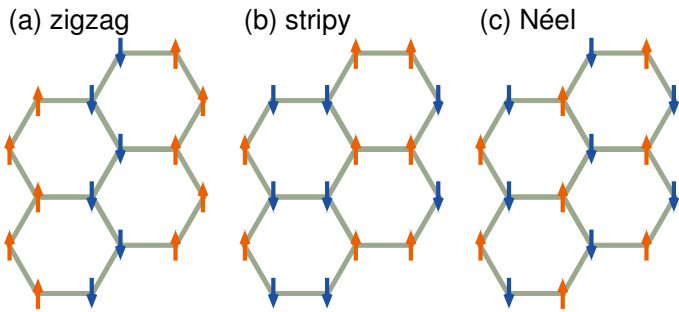


FIG. 2: Possible antiferromagnetic patterns in a honeycomb lattice

As shown by transport, optical and high-energy spectroscopy studies<sup>10,11</sup>,  $\text{Na}_2\text{IrO}_3$  is an insulator with an energy gap  $E_g$  of 340 meV. Magnetic susceptibility measurements indicate a Curie-Weiss behavior at high temperatures with a Curie-Weiss temperature  $\Theta_{CW} = -116$  K and an effective Ir moment  $\mu_{\text{eff}} = 1.82\mu_B$ .  $\text{Na}_2\text{IrO}_3$  orders antiferromagnetically below  $T_N = 15$  K with an ordered magnetic moment  $\mu_{\text{ord}} \sim 0.2\mu_B$ . The fact that  $T_N$  is much smaller than  $\Theta_{CW}$  may be a signature of frustration, but it may be also caused by the itinerancy of Ir 5d electrons<sup>5</sup> as will be discussed in Section VI.

The magnetic pattern observed experimentally<sup>8</sup> corresponds to a zigzag ordering, in contrast to the prediction of a stripe order by the nnKH model<sup>2</sup> (see Fig. 2). Recently, Chaloupka *et al.*<sup>4</sup> argued that such a zigzag ordering can be also obtained by the nnKH model, when one correctly includes all the terms contributing to NN Ir-Ir exchange. In Section V, we will discuss this proposition in more detail.

### III. METHOD

In this work we perform DFT calculations using the linearized augmented plane wave (LAPW) method as implemented in the full-potential code WIEN2k<sup>12</sup>. We employ the Perdew-Burke-Ernzerhof generalized gradient approximation<sup>13</sup> to the DFT exchange-correlation functional and set the basis-size controlling parameter  $RK_{\text{max}}$ <sup>14</sup> to 7. We consider a mesh of 500  $\mathbf{k}$ -points in the first Brillouin zone. Relativistic effects are treated within the second variational approach. Convergence with respect to relevant parameters (the  $\mathbf{k}$ -point mesh, the  $RK_{\text{max}}$  and the second variational energy cutoff, *etc.*) has been carefully checked.

#### A. Calculation of hopping integrals

In order to be able to discuss various Ir-Ir 5d processes, we parameterize our non-relativistic DFT results in terms of a tight-binding (TB) model where the TB Ir 5d hop-

ping parameters are obtained through the Wannier function projection formalism proposed in Ref. 15 and generalized to molecular Wannier functions in Ref. 16. We first construct Wannier function projectors  $P_{m\nu}^\alpha(\mathbf{k})$  for the three  $t_{2g}$  Ir 5d orbitals and calculate the TB Hamiltonian  $H^{\text{TB}}(\mathbf{k})$  (in matrix form) via

$$H^{\text{TB}}(\mathbf{k}) = P(\mathbf{k})D(\mathbf{k})P^\dagger(\mathbf{k}), \quad (2)$$

where  $D(\mathbf{k})$  is a diagonal matrix of Ir 5d  $t_{2g}$  Bloch eigenvalues and the matrix  $P(\mathbf{k})$  is formed by the projectors  $P_{m\nu}^\alpha(\mathbf{k})$ . Here, indices  $\alpha$ ,  $m$ , and  $\nu$  run over equivalent Ir atoms in the unit cell, Ir  $t_{2g}$  orbitals, and Bloch bands, respectively.  $\text{Na}_2\text{IrO}_3$  has two Ir per unit cell and only the six Ir  $t_{2g}$  bands near the Fermi level  $E_F$  are considered in the construction of projectors.

We calculate the hopping integral  $t_{\alpha-\mathbf{R},\alpha'-\mathbf{R}'}^{mm'}$  between orbital  $m$  on Ir atom  $\alpha$  in the unit cell at a distance  $\mathbf{R}$  from a reference unit cell and orbital  $m'$  on Ir atom  $\alpha'$  in the unit cell at a distance  $\mathbf{R}'$  from a reference unit cell by integrating  $H^{\text{TB}}(\mathbf{k})$  over  $N_{\mathbf{k}}$   $\mathbf{k}$ -vectors in the first Brillouin zone:

$$t_{\alpha-\mathbf{R},\alpha'-\mathbf{R}'}^{mm'} = \frac{1}{N_{\mathbf{k}}} \sum_{\mathbf{k}} H_{\alpha m, \alpha' m'}^{\text{TB}}(\mathbf{k}) e^{-i\mathbf{k}(\mathbf{R}-\mathbf{R}')}. \quad (3)$$

where  $H_{\alpha m, \alpha' m'}^{\text{TB}}(\mathbf{k})$  are the matrix elements of  $H^{\text{TB}}(\mathbf{k})$ . Correspondingly, the diagonal matrix elements  $t_{\alpha\alpha}^{mm}$  give the on-site energies.

#### B. Construction of quasi-molecular projectors

As was argued in Ref. 5, the most natural description of the electronic structure of  $\text{Na}_2\text{IrO}_3$  is in terms of quasi-molecular (QMO) orbitals localized on a hexagon. The strongest Ir-Ir hopping is between 5d  $t_{2g}$  orbitals of neighboring iridium ions via common oxygens. In this case, an electron on a given Ir  $t_{2g}$  orbital propagates around an  $\text{Ir}_6$  hexagon with the peculiarity that only a certain  $t_{2g}$  orbital at each Ir participates in the hopping<sup>17</sup>, e.g.  $\text{Ir1}(xy)\text{-Ir2}(xz)\text{-Ir3}(yz)\text{-Ir4}(xy)\text{-Ir5}(xz)\text{-Ir6}(yz)$  (see Fig. 2 of Ref. 5). These QMOs are analogous to the molecular orbitals of the benzene molecule  $\text{C}_6\text{H}_6$  except for the fact that in benzene the same  $p$ -orbital on each carbon ion participates in the formation of the molecular orbital while in  $\text{Na}_2\text{IrO}_3$ , as described above, different  $t_{2g}$  orbitals are involved in one QMO and the three  $t_{2g}$  orbitals on one Ir ion contribute to three different neighboring QMOs. We elaborate the details of the construction of the QMOs in what follows.

QMO projectors  $P_{M\nu}(\mathbf{k})$  are obtained as linear combinations of Ir  $t_{2g}$  projectors  $P_{M\nu}(\mathbf{k})$ :

$$P_{M\nu}(\mathbf{k}) = \sum_M U_{M,M} T_M(\mathbf{k}) P_{M\nu}(\mathbf{k}). \quad (4)$$

where in the Ir  $t_{2g}$  projectors  $P_{M\nu}(\mathbf{k})$ , the index  $M$  combines now the atomic index  $\alpha$  and orbital index  $m$ , *i.e.*  $M$

runs over all  $t_{2g}$  orbitals of all equivalent Ir atoms. With QMOs ordered as  $\mathcal{M} = A_{1g}, E_{2u}, E_{1g}, B_{1u}, E_{1g}, E_{2u}$  and Ir  $t_{2g}$  orbitals ordered as  $M = xy^1, xz^1, yz^1, xy^2, xz^2, yz^2$  (the upper index labels Ir atoms),  $U$  is given by  $[\omega = \exp(i\pi/3)]$

$$U = \begin{pmatrix} 1 & 1 & 1 & 1 & 1 & 1 \\ 1 & \omega^4 & \omega^2 & -1 & \omega & \omega^5 \\ 1 & \omega^2 & \omega^4 & 1 & \omega^2 & \omega^4 \\ 1 & 1 & 1 & -1 & -1 & -1 \\ 1 & \omega^4 & \omega^2 & 1 & \omega^4 & \omega^2 \\ 1 & \omega^2 & \omega^4 & -1 & \omega^5 & \omega \end{pmatrix}, \quad (5)$$

and  $T_M(\mathbf{k})$  are the Bloch factors, accounting for the fact that the 6 sites forming a QMO belong to several different unit cells. Actual values for these factors depend on the manner in which a particular band structure code selects the unit cell (see the Appendix for the WIEN2k settings).

#### IV. NON-RELATIVISTIC ELECTRONIC STRUCTURE

In this Section we analyze and discuss the Ir-Ir  $5d$   $t_{2g}$  tight-binding parameters for  $\text{Na}_2\text{IrO}_3$  *up to second nearest neighbors*. As mentioned in Section II, three structural distortions are present in  $\text{Na}_2\text{IrO}_3$ : orthorhombic distortion,  $\text{IrO}_6$  octahedra rotation and trigonal distortion. Besides, the stacking of the honeycomb planes inherently violates the rhombohedral symmetry even if each plane is ideal. The formation of QMOs relies on the dominance of *intra*hexagon hopping<sup>5</sup> and therefore is sensitive to structural details. Therefore it is important to understand the role of structural distortions in establishing electron hopping paths. This motivates us to study electronic properties of a number of artificially idealized  $\text{Na}_2\text{IrO}_3$  unit cells where structural distortions of different types are systematically eliminated<sup>20</sup>. Such a procedure has proven very useful<sup>21</sup> in understanding the behavior of  $\text{Sr}_2\text{IrO}_4$ .

We consider four different crystal structures: (i) the experimental crystal structure<sup>8</sup>,  $S_{\text{exp}}$ , (ii) an artificially idealized  $\text{Na}_2\text{IrO}_3$  unit cell,  $S_1$ , where the orthorhombic distortion has been removed from the experimental crystal structure, (iii) an artificially idealized  $\text{Na}_2\text{IrO}_3$  unit cell,  $S_2$ , where the  $\text{IrO}_6$  octahedra rotations have been removed from  $S_1$ , and (iv) an artificially idealized  $\text{Na}_2\text{IrO}_3$  unit cell,  $S_3$ , where the trigonal distortion has been removed from  $S_2$ . Table I shows a comparison of total (non-magnetic) DFT energies for the various structures. As it is to be expected, the experimental structure is the energetically most stable case. Tight-binding hopping parameters between Ir  $t_{2g}$  orbitals up to second nearest neighbors calculated for the four structures are given in Table II and schematically represented in Fig. 3. We consider the following rationale for labeling of the hopping parameters Eq. 3. In the experimental structure of  $\text{Na}_2\text{IrO}_3$  there are two first NN Ir-Ir distances and two second NN Ir-Ir distances due to the fact that the Ir<sub>6</sub>

| Structure                                     | $S_{\text{exp}}$ | $S_1$ | $S_2$ | $S_3$  |
|---|------------------|-------|-------|--------|
| $E_{S_i} - E_{S_{\text{exp}}} \text{ (mRyd)}$ | 0                | 0.95  | 78.90 | 180.01 |

TABLE I: Non-relativistic total energies obtained within DFT for the experimental,  $E_{S_{\text{exp}}}$ , and the three idealized,  $S_i$  ( $i = 1, 2, 3$ ),  $\text{Na}_2\text{IrO}_3$  crystal structures. Energy is given per unit cell containing two formula units.

hexagons are not perfect. We denote the corresponding Ir  $t_{2g}$  - Ir  $t_{2g}$  hopping parameters as  $t_1$  and  $t_{\bar{1}}$  for the first NN and, respectively,  $t_2$  and  $t_{\bar{2}}$  for the second NN hoppings. Further, we have various possible hoppings between equal and different  $t_{2g}$  orbitals. Regarding first NN, we denote  $t_{1\text{O}}$  and  $t_{\bar{1}\text{O}}$  the hoppings between unlike  $t_{2g}$  orbitals via O  $p$  states (Fig. 3 (a)).  $t_{1\sigma}$  and  $t_{\bar{1}\sigma}$  denote NN direct hoppings of  $\sigma$ -type.  $t_{1\parallel}$  and  $t_{\bar{1}\parallel}$  denote NN hoppings between like orbitals lying in parallel planes. In the ideal structure such hoppings consist of linear combinations with equal weight of  $dd\pi$  and  $dd\delta$  bonds.  $t_{1\perp}$  and  $t_{\bar{1}\perp}$  denote NN hoppings between unlike orbitals lying in perpendicular planes (see Figs. 3 (b) and (c)).

Regarding the second NN hopping parameters,  $t_{2\text{O}}$  and  $t_{\bar{2}\text{O}}$  denote hoppings between unlike orbitals via O  $p$  and Na  $s$  states (Fig. 3 (e)).  $t_{2a}$  and  $t_{2b}$  ( $t_{\bar{2}a}$  and  $t_{\bar{2}b}$ ) denote hoppings between like orbitals as shown in Fig. 3 (d) and  $t_{2c}$ ,  $t_{2d}$  and  $t_{2e}$  ( $t_{\bar{2}c}$ ,  $t_{\bar{2}d}$  and  $t_{\bar{2}e}$ ) denote hoppings between unlike orbitals (Fig. 3 (e)).

##### A. Experimental crystal structure

Previous electronic structure calculations<sup>5</sup> have identified the dominant hopping integrals for  $\text{Na}_2\text{IrO}_3$  to be  $t_{1\text{O}}$  and  $t_{2\text{O}}$  [as well as  $t_{\bar{1}\text{O}}$  and  $t_{\bar{2}\text{O}}$ ; further on, if not explicitly stated otherwise, we refer to both equivalent  $t_1$  ( $t_2$ ) and  $t_{\bar{1}}$  ( $t_{\bar{2}}$ ) when writing  $t_1$  ( $t_2$ )]. In Table II column  $S_{\text{exp}}$  we present the complete list of hopping parameters up to the second nearest neighbors. A TB model based only on these hopping integrals provides already a reasonable description of  $\text{Na}_2\text{IrO}_3$  Ir  $t_{2g}$  states near the Fermi level  $E_F$  [Fig. 4 (a)].

We first note a very good agreement between the  $t_{1\text{O}}$  ( $\sim 270$  meV) and  $t_{2\text{O}}$  ( $\sim -75$  meV) values obtained with our WIEN2k-based projection method and with the FPLO code<sup>18</sup> as was used in Ref. 5. These leading Ir  $t_{2g}$  hoppings strongly tend to confine the electron's motion to a single Ir hexagon and, as a result, the electronic structure of  $\text{Na}_2\text{IrO}_3$  near the Fermi level is dominated by the formation of well separated and relatively weakly dispersive QMOs<sup>5</sup>. On an Ir hexagon, as shown above, each Ir atom participates with one of its  $t_{2g}$  orbitals (see Fig. 2 of Ref. 5). These orbitals combine to form six QMOs according to the unitary transformation Eq. (5). In support of this picture, Fig. 5 (a) shows the density of states of  $\text{Na}_2\text{IrO}_3$  projected onto the six QMOs (singlets  $A_{1g}$  and  $B_{1u}$  and doublets  $E_{2u}$  and  $E_{1g}$ ), where states

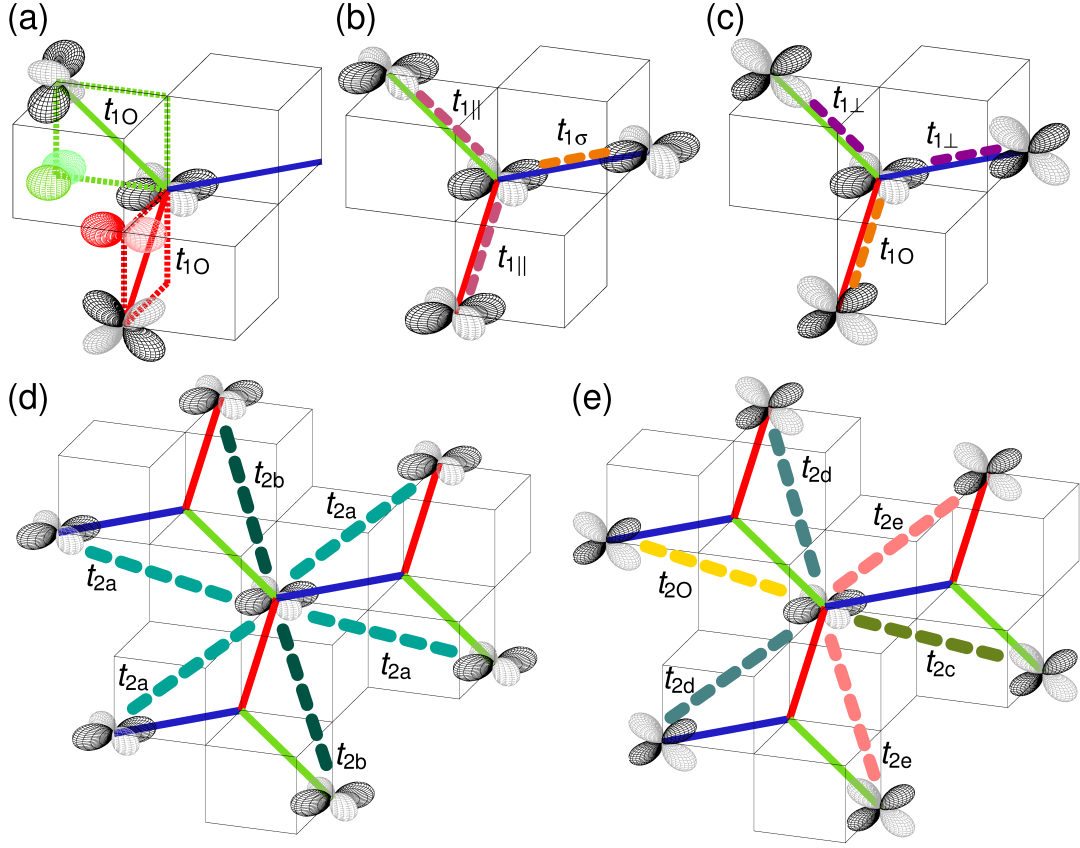


FIG. 3: Schematic representation of Ir-Ir  $t_{2g}$  hopping paths up to second nearest neighbor in  $\text{Na}_2\text{IrO}_3$ .

with certain predominant QMO character are clearly separated in energy from one another. The near-degeneracy of  $A_{1g}$  and  $E_{2u}$  states around  $E_F$  is rather accidental resulting from the  $t_{1O}/t_{2O} \sim -3.6$  ratio (see Table II and Ref. 5). The real-space representations of the QMO Wannier functions onto which the  $\text{Na}_2\text{IrO}_3$  DOS is being projected are shown in Fig. 6. The QMO Wannier functions were constructed as described in Section II by explicitly accounting for the location of each Ir  $t_{2g}$  orbital in the crystal<sup>19</sup>.

Other NN and second NN hopping processes involving intraorbital and interorbital hoppings (see Table II) allow an electron to jump from one QMO to another and hence are responsible for the band dispersion. Many of those hoppings are of the same order of magnitude (although mostly by at least an order of magnitude smaller) than  $t_{2O}$ , like, for example,  $t_{1||}$  and  $t_{1\perp}$ . For the “z” bond such hoppings will be between  $xz$  and  $xz$  or  $yz$  and  $yz$  orbitals (see Fig. 3 (b)). These hoppings are equal to 47.7, 30.0, and 33.1 meV, depending on the NN bond (see Table II). In fact, such appreciable variations in magnitude, which violate the  $D_{6h}$  symmetry of an ideal Ir hexagon, are ubiquitous among the hoppings that connect neighboring QMOs. Some of them even change sign, as, for instance  $t_{1\sigma}$  and  $t_{1\bar{\sigma}}$ . This feature results from the orthorhombic stacking, distortions within the  $\text{Ir}_2\text{Na}$  planes, and rota-

tions of  $\text{IrO}_6$  octahedra.

### B. Structure $S_1$ obtained by removing the orthorhombic distortion

We now consider an idealized  $\text{Na}_2\text{IrO}_3$  structure without the orthorhombic distortion of Ir hexagons; this structure, which we call  $S_1$ , as well as other structures in this Section, is tabulated in the Appendix. In the structure  $S_1$ : (i) all *intralayer* Ir-Ir bonds are of the same length, *i.e.*, the  $D_{6h}$  symmetry of an Ir hexagon is restored, (ii) all NN Ir-O bonds are of the same length, (iii) all Ir-O-Ir bond angles are equal to  $98.7^\circ$ , and (iv) the oxygens lie on the faces of a cube drawn around an Ir hexagon (see Fig. 2 of Ref. 5). The 3D crystal structure, though, remains orthorhombic in this approximation, due to the presence of multiple Ir layers. This explains small residual variations among the nominally equivalent TB model parameters (Table II, column  $S_1$ ): *E.g.*, comparing parameters labeled with and without overbar; also, onsite energies like the  $xy$  on-site energy is slightly lower than the  $xz/yz$  on-site energy. However, these variations of  $t_{2g}$  orbital on-site energies, as well as of equivalent hopping integrals, are now noticeably smaller than in the experimental  $\text{Na}_2\text{IrO}_3$  structure.



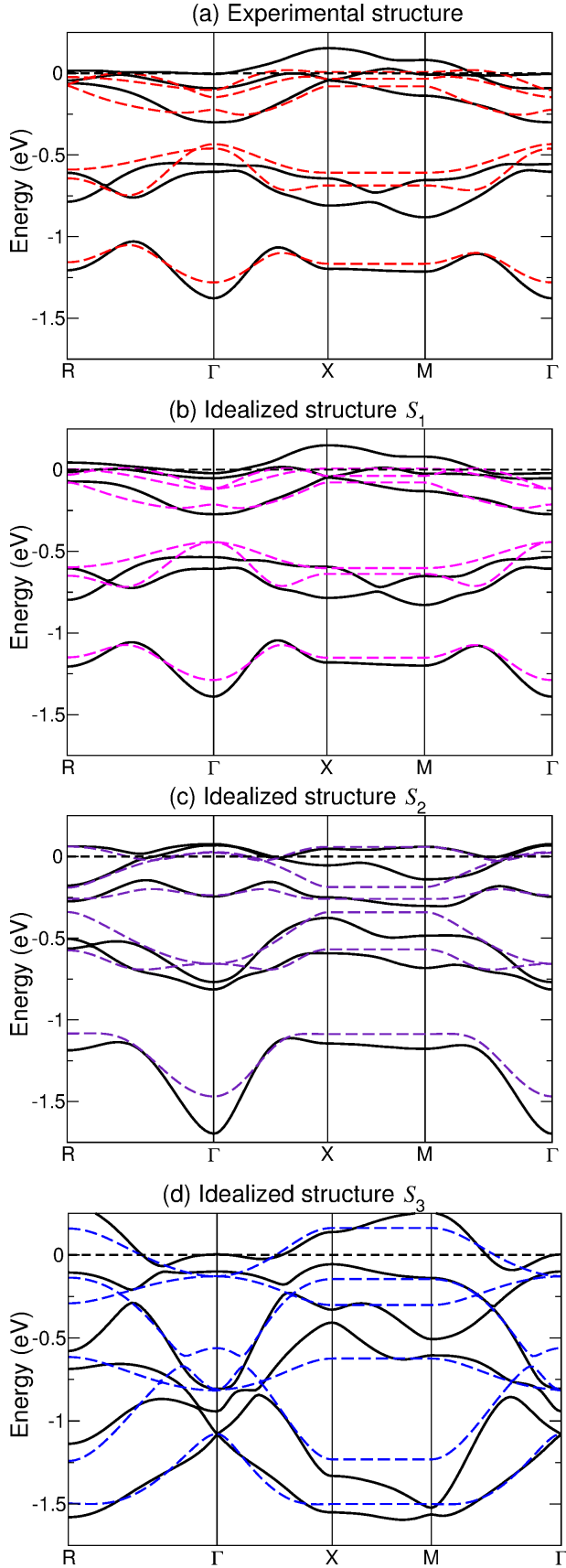


FIG. 4:  $\text{Na}_2\text{IrO}_3$  bandstructures near the Fermi level  $E_F = 0$  calculated using DFT (black solid lines) and a TB model that considers *only* up to NNN hopping processes between Ir  $t_{2g}$  orbitals (dashed lines). The data are obtained with (a) experimental crystal structure and idealized structures (b)  $S_1$ , (c)  $S_2$ , and (d)  $S_3$ .

TABLE II: Nearest neighbor (NN) and second NN hopping integrals in meV between Ir  $t_{2g}$  orbitals for the experimental structure and three idealized structures  $S_1$ ,  $S_2$ ,  $S_3$  of  $\text{Na}_2\text{IrO}_3$  (see text and Appendix for a description of the structures and parameter labeling). The NN = 0 data are Ir  $t_{2g}$  on-site energies and *interorbital* hoppings; the NN = 1 and NN =  $\bar{1}$  (NN = 2 and NN =  $\bar{2}$ ) data are hoppings over nonequivalent (due to orthorhombic distortion) NN (second NN) Ir bonds.

| NN        |   | $S_{exp}$ | $S_1$  | $S_2$  | $S_3$  |
|-----------|---|-----------|--------|--------|--------|
| 0         | $xy \rightarrow xy$   | -448.8    | -422.9 | -422.8 | -601.1 |
|           | $xz \rightarrow xz$   | -421.5    | -421.8 | -421.2 | -601.1 |
|           | $yz \rightarrow yz$   | -421.5    | -421.8 | -421.2 | -601.1 |
|           | $xy \rightarrow xz, xy \rightarrow yz$                        | -27.8     | -26.4  | -21.2  | -13.5  |
|           | $xz \rightarrow yz$   | -23.1     | -25.2  | -18.8  | -14.7  |
| 1         | $xy \rightarrow xy (t_{1\parallel})$                          | 47.7      | 34.1   | 27.8   | 120.8  |
|           | $xy \rightarrow xz, xy \rightarrow yz (t_{1O})$               | 269.6     | 268.5  | 231.7  | 209.7  |
|           | $xy \rightarrow xz, xy \rightarrow yz (t_{1\perp})$           | -25.6     | -16.6  | 43.7   | -5.3   |
|           | $xz \rightarrow xz, yz \rightarrow yz (t_{1\parallel})$       | 30.0      | 33.2   | 17.2   | 118.9  |
|           | $xz \rightarrow xz, yz \rightarrow yz (t_{1\sigma})$          | -20.7     | 3.5    | -66.5  | -381.6 |
| $\bar{1}$ | $xz \rightarrow yz (t_{1\perp})$                              | -21.4     | -16.4  | 41.7   | -4.9   |
|           | $xy \rightarrow xy (t_{\bar{1}\sigma})$                       | 25.4      | 0.2    | -65.5  | -382.8 |
|           | $xy \rightarrow xz, xy \rightarrow yz (t_{\bar{1}\perp})$     | -11.9     | -17.6  | 46.9   | -5.3   |
|           | $xz \rightarrow xz, yz \rightarrow yz (t_{\bar{1}\parallel})$ | 33.1      | 33.9   | 21.2   | 120.5  |
|           | $xz \rightarrow yz (t_{\bar{1}O})$                            | 264.4     | 264.8  | 228.7  | 211.7  |
| 2         | $xy \rightarrow xy (t_{2a})$                                  | -3.5      | -2.6   | -18.9  | 2.0    |
|           | $xy \rightarrow xz, xy \rightarrow yz (t_{2O})$               | -75.8     | -77.4  | -94.7  | -82.1  |
|           | $xy \rightarrow xz, xy \rightarrow yz (t_{2c})$               | -36.5     | -35.3  | -52.1  | -38.5  |
|           | $xy \rightarrow xz, xy \rightarrow yz (t_{2d})$               | 12.5      | 10.1   | 1.7    | 6.9    |
|           | $xy \rightarrow xz, xy \rightarrow yz (t_{2e})$               | -21.4     | -19.2  | -7.3   | 1.9    |
|           | $xz \rightarrow xz, yz \rightarrow yz (t_{2a})$               | -0.6      | -3.1   | -16.6  | 1.4    |
|           | $xz \rightarrow xz, yz \rightarrow yz (t_{2b})$               | -1.5      | -1.6   | -1.0   | 5.7    |
|           | $xz \rightarrow yz (t_{2e})$                                  | -18.6     | -19.0  | -7.1   | 2.4    |
| $\bar{2}$ | $xz \rightarrow yz (t_{2d})$                                  | 10.2      | 10.2   | 2.4    | 6.6    |
|           | $xy \rightarrow xy (t_{\bar{2}b})$                            | -1.4      | -1.4   | -1.2   | 5.7    |
|           | $xy \rightarrow xz, xy \rightarrow yz (t_{\bar{2}e})$         | -19.0     | -19.2  | -8.4   | 2.1    |
|           | $xy \rightarrow xz, xy \rightarrow yz (t_{\bar{2}d})$         | 9.3       | 10.2   | 0.7    | 7.5    |
|           | $xz \rightarrow xz, yz \rightarrow yz (t_{\bar{2}a})$         | -1.4      | -3.0   | -17.7  | 1.5    |
|           | $xz \rightarrow yz (t_{\bar{2}O})$                            | -77.0     | -78.0  | -95.2  | -81.9  |
|           | $xz \rightarrow yz (t_{\bar{2}c})$                            | -30.4     | -35.1  | -51.6  | -38.9  |

We conclude that removal of the orthorhombic distortion restores (to a certain degree) the degeneracy of the Ir  $t_{2g}$  orbitals, but does not change the hierarchy of hopping integrals. In the structure  $S_1$ , the  $t_{1O}$  and  $t_{2O}$  values are close to the respective values in the experimental  $\text{Na}_2\text{IrO}_3$  structure and, as a consequence, the overall structure of the  $t_{2g}$  bands is only slightly changed [Figs. 4 (b) and 5 (b)].

### C. Structure $S_2$ obtained by removing the $\text{IrO}_6$ octahedra rotations

In the structure  $S_1$  that we designed in the previous Section, two types of distortions are still present: (i) trigonal squeezing of  $\text{IrO}_6$  octahedra along the (111) direc-

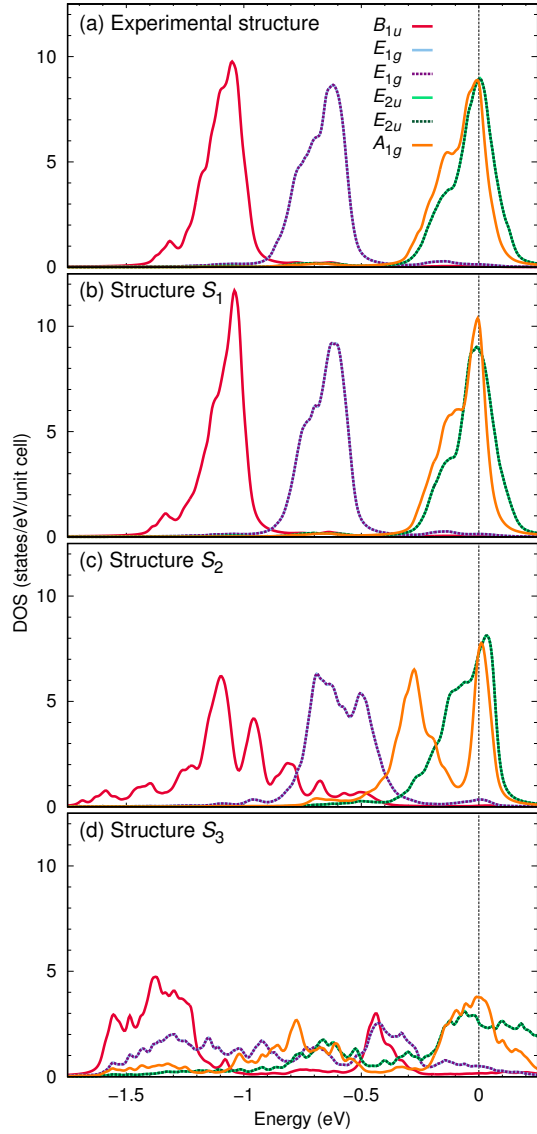


FIG. 5:  $\text{Na}_2\text{IrO}_3$  DOS projected onto QMOs for (a) experimental crystal structure and idealized structures (b)  $S_1$ , (c)  $S_2$ , and (d)  $S_3$ . The Fermi level is set to zero.

tion perpendicular to Ir hexagon planes and (ii)  $\text{IrO}_6$  octahedra rotations that place O atoms on the cube's faces. We now consider structure  $S_2$ , where the  $\text{IrO}_6$  octahedra rotations are removed from  $S_1$ . In this structure, the Na-O and Ir-O bond lengths are the same (in the experimental structure, the former is considerably longer). This feature enhances the second NN hopping processes through Na  $s$  states, such as  $t_{2O}$ ,  $t_{2a}$ ,  $t_{2c}$  (and the equivalent overbar hoppings) as shown in Table II, column  $S_2$ . At the same time, the NN O-assisted hopping  $t_{1O}$  gets reduced and the  $t_{1O}/t_{2O}$  ratio decreases to  $\sim -2.4$ , resulting in a larger separation of the lowest ( $B_{1u}$ ) band from the rest of  $t_{2g}$  bands [Fig. 4 (c)]. Formation of QMOs still takes place in structure  $S_2$  [Fig. 5 (c)], but the

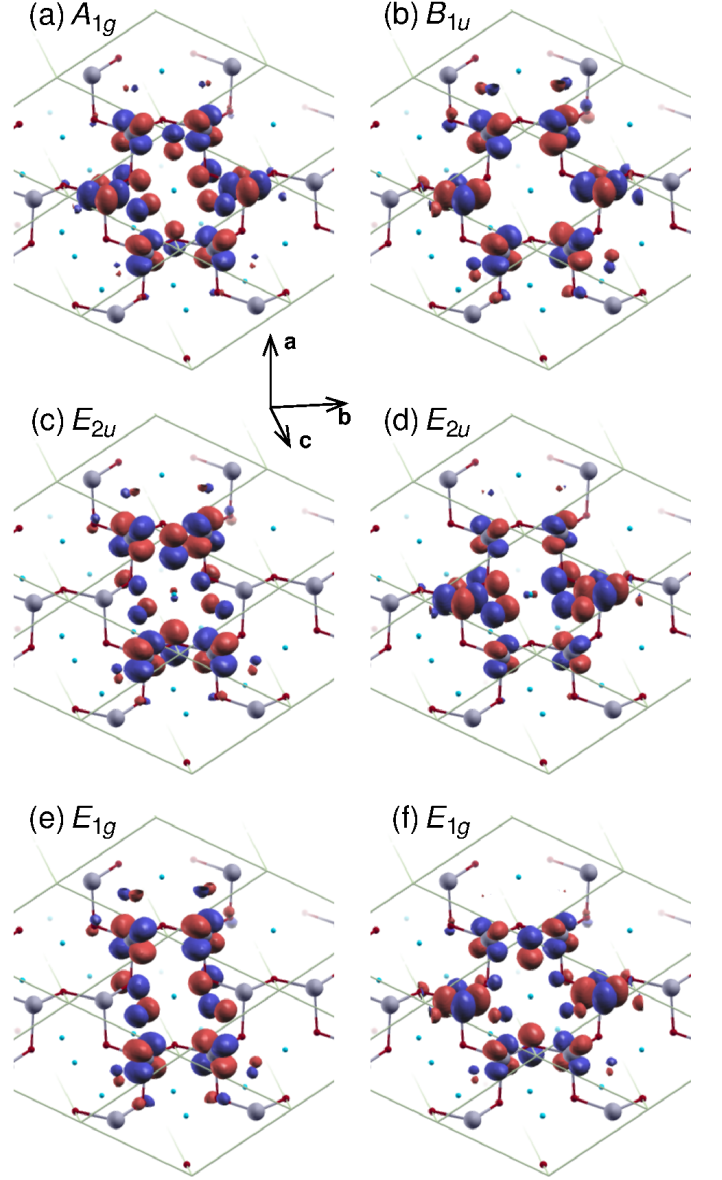


FIG. 6: Real-space representation of the QMOs in  $\text{Na}_2\text{IrO}_3$  obtained by the Wannier projector method.

QMO bands are more dispersive compared to the experimental or  $S_1$  structures, due to increased *interhexagon* NN hopping integrals  $t_{1\sigma}$ ,  $t_{1\perp}$  (and equivalent  $t_{\bar{1}\sigma}$ ,  $t_{\bar{1}\perp}$ ): thus, one observes broadening of the  $A_{1g}$  band and redistribution of weight away from the  $E_{2u}$  doublet.

#### D. Structure $S_3$ obtained by removing the trigonal distortion

We finally consider a most idealized  $\text{Na}_2\text{IrO}_3$  structure  $S_3$  without the trigonal distortion, *i.e.*, with  $90^\circ$  Ir-O-Ir bond angles. Importantly, one can only remove this distortion, while keeping the Ir-O bond length the same, if

the Ir-Ir bonds are shortened. Because of that, the hierarchy of hopping integrals changes drastically (Table II, column  $S_3$ ). The dominant hopping is now the direct NN hopping between like orbitals  $t_{1\sigma}$  (and the equivalent  $t_{\bar{1}\sigma}$ ) reaching  $\sim -380$  meV, while the O-assisted hopping  $t_{1O}$  ( $t_{\bar{1}O}$ ) has been reduced to  $\sim 210$  meV. Accordingly, the large *interhexagon* interaction destroys the QMO picture, as illustrated by the strongly dispersive  $t_{2g}$  manifold in Fig. 4 (d) and the delocalization of individual QMO characters over the whole DOS range in Fig. 5 (d). We also observe that the main reason for the trigonal squeeze is the geometrical effect of optimizing simultaneously the Ir-Ir and Ir-O bonds. As a result, even though the on-site  $t_{2g}$  orbitals split into an  $a_{1g}$  singlet and an  $e_g$  doublet, this is not a strong effect and not the driving force for the squeeze, as it is often assumed in the spirit of localized limit and the Jahn-Teller effect.

Summarizing these results, in the  $S_3$  structure, the NN direct hopping increases by an order of magnitude compared to the experimental  $\text{Na}_2\text{IrO}_3$  structure and the NN O-assisted hoppings get suppressed. Therefore we conclude that structural distortions of all types in  $\text{Na}_2\text{IrO}_3$  act constructively to enhance the *intrahexagon* effective hopping parameters (such as  $t_{1O}$  and  $t_{2O}$ ) and suppress the *interhexagon* ones (such as NN direct hopping) favoring the formation of QMOs.

## V. SPIN-ORBIT COUPLING

We proceed now with the analysis of the electronic structure of  $\text{Na}_2\text{IrO}_3$  in the presence of spin-orbit (SO) coupling. Previous relativistic DFT calculations<sup>22</sup> showed that  $\text{Na}_2\text{IrO}_3$  states near the Fermi level experience strong relativistic splitting with pronounced concentration of  $j_{\text{eff}} = \frac{1}{2}$  character in the upper two bands. However, the  $\text{Na}_2\text{IrO}_3$  relativistic states seem to preserve their QMO identity as well [see Fig. S6 (b) of Ref. 5]. In order to understand such duality, we set up a TB model for the Ir  $t_{2g}$  orbitals that includes also local SO interaction terms. With this TB+SO model, we are able not only to confirm the relativistic DFT results by calculating DOS but also to access the composition of individual states and trace their evolution as a function of the spin-orbit coupling  $\lambda$ .

### A. TB+SO model

We start with a TB model that perfectly describes the non-relativistic DFT Ir  $t_{2g}$  bands of  $\text{Na}_2\text{IrO}_3$ . It includes three hundred and twenty one hopping integrals between up to 50 nearest neighbors. We then double the dimension of the TB Hamiltonian matrix to introduce spin dependence and add local SO coupling terms  $\langle \lambda \mathbf{L} \cdot \mathbf{S} \rangle$  that

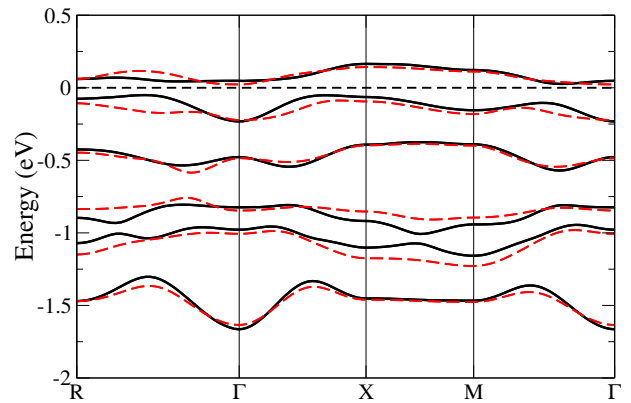


FIG. 7: WIEN2k relativistic bandstructure (black solid lines) versus TB+SO model relativistic bandstructure (red dashed lines) of  $\text{Na}_2\text{IrO}_3$  as described in the text. In model calculations,  $\lambda = 0.44$  eV was used.

mix spin- $\uparrow$  and spin- $\downarrow$  subspaces:

|                 | $xy \uparrow$        | $xz \uparrow$         | $yz \uparrow$         | $xy \downarrow$      | $xz \downarrow$      | $yz \downarrow$       |
|-----------------|----------------------|-----------------------|-----------------------|----------------------|----------------------|-----------------------|
| $xy \uparrow$   | 0                    | 0                     | 0                     | 0                    | $\frac{\lambda}{2}$  | $-\frac{i\lambda}{2}$ |
| $xz \uparrow$   | 0                    | 0                     | $\frac{i\lambda}{2}$  | $-\frac{\lambda}{2}$ | 0                    | 0                     |
| $yz \uparrow$   | 0                    | $-\frac{i\lambda}{2}$ | 0                     | $\frac{i\lambda}{2}$ | 0                    | 0                     |
| $xy \downarrow$ | 0                    | $-\frac{\lambda}{2}$  | $-\frac{i\lambda}{2}$ | 0                    | 0                    | 0                     |
| $xz \downarrow$ | $\frac{\lambda}{2}$  | 0                     | 0                     | 0                    | 0                    | $-\frac{i\lambda}{2}$ |
| $yz \downarrow$ | $\frac{i\lambda}{2}$ | 0                     | 0                     | 0                    | $\frac{i\lambda}{2}$ | 0                     |

(6)

Importantly, even though SO coupling is a local on-site interaction, it couples neighboring quasi-molecular orbitals and therefore is  $\mathbf{k}$ -vector dependent in the QMO basis.

Having thus set up the TB model, we vary the SO coupling strength  $\lambda$  until the best matching with the DFT relativistic bands is achieved, which is found to correspond to  $\lambda = 0.44$  eV (Fig. 7).

Since our purpose is to reconcile the QMO and relativistic orbital (RO) pictures, we analyze the  $\lambda \mathbf{L} \cdot \mathbf{S}$  matrix elements between spin- $\uparrow$  and spin- $\downarrow$  QMOs to see how SO coupling mixes QMO characters. They can be easily obtained by applying the unitary transformation  $UT(\mathbf{k})$  [Eq. (5)] to the  $\lambda \mathbf{L} \cdot \mathbf{S}$  matrix in the  $t_{2g}$  basis:

$$H_{\text{QMO}}^{\text{SO}}(\mathbf{k}) = UT(\mathbf{k}) H_{t_{2g}}^{\text{SO}} T^H(\mathbf{k}) U^H. \quad (7)$$

This equation explicitly illustrates how  $\mathbf{k}$ -vector dependence enters the SO matrix elements in the QMO basis. Concise expressions can be derived if one notes that QMOs can be represented by their “winding number”  $n$  which defines a phase change  $\Delta\phi = \frac{n\pi}{3}$  of  $t_{2g}$  orbitals around a hexagon. In this notation, QMOs  $A_{1g}, E_{2u}, E_{1g}, B_{1u}, E_{1g}, E_{2u}$  correspond to, respectively,  $n = 0, 1, 2, 3, 4, 5$  winding numbers. The  $\lambda \mathbf{L} \cdot \mathbf{S}$  matrix



elements in the QMO basis are given then by

$$\begin{aligned}
H_{n\uparrow n'\uparrow}^{\text{SO}} = & \frac{\lambda}{2} i e^{\frac{(n'-n)\pi i}{2}} \cos \frac{(n'-n)\pi}{2} \cos(k_x + k_y) \\
& \times \left( e^{\frac{2(2n'-n)\pi i}{3}} - e^{-\frac{2(2n-n')\pi i}{3}} \right) \\
& + \frac{\lambda}{2} i e^{\frac{(n'-n)\pi i}{2}} \sin \frac{(n'-n)\pi}{2} \sin(k_x + k_y) \\
& \times \left( e^{\frac{2(2n'-n)\pi i}{3}} + e^{-\frac{2(2n-n')\pi i}{3}} \right)
\end{aligned} \quad (8)$$

and

$$\begin{aligned}
H_{n\uparrow n'\downarrow}^{\text{SO}} = & 2 e^{\frac{(n'-n)\pi i}{2}} \left( e^{\frac{4n'\pi i}{3}} \cos\left(-\frac{(n'-n)\pi}{2} + k_y\right) \right. \\
& - e^{-\frac{4n\pi i}{3}} \cos\left(-\frac{(n'-n)\pi}{2} - k_y\right) \\
& + i e^{\frac{2n'\pi i}{3}} \cos\left(-\frac{(n'-n)\pi}{2} - k_x\right) \\
& \left. - i e^{-\frac{2n\pi i}{3}} \cos\left(-\frac{(n'-n)\pi}{2} + k_x\right) \right).
\end{aligned} \quad (9)$$

We list numerical values of the matrix elements for two representative  $\mathbf{k}$ -vectors:  $\mathbf{k} = (0, 0, 0)$  (point  $\Gamma$ ) (first two tables) and  $\mathbf{k} = (\frac{\pi}{2}, 0, 0)$  (last two tables).

|                   | $n=5$             | $n=0$             | $n=1$             | $n=2$             | $n=3$             | $n=4$             |
|-------------------|-------------------|-------------------|-------------------|-------------------|-------------------|-------------------|
|                   | $E_{2u} \uparrow$ | $A_{1g} \uparrow$ | $E_{2u} \uparrow$ | $E_{1g} \uparrow$ | $B_{1u} \uparrow$ | $E_{1g} \uparrow$ |
| $E_{2u} \uparrow$ | $C_1$             | 0                 | 0                 | 0                 | $-C_1$            | 0                 |
| $A_{1g} \uparrow$ | 0                 | 0                 | 0                 | $-C_1$            | 0                 | $C_1$             |
| $E_{2u} \uparrow$ | 0                 | 0                 | $-C_1$            | 0                 | $C_1$             | 0                 |
| $E_{1g} \uparrow$ | 0                 | $-C_1$            | 0                 | $C_1$             | 0                 | 0                 |
| $B_{1u} \uparrow$ | $-C_1$            | 0                 | $C_1$             | 0                 | 0                 | 0                 |
| $E_{1g} \uparrow$ | 0                 | $C_1$             | 0                 | 0                 | 0                 | $-C_1$            |

(10)

|                   | $n=5$               | $n=0$               | $n=1$               | $n=2$               | $n=3$               | $n=4$               |
|-------------------|---------------------|---------------------|---------------------|---------------------|---------------------|---------------------|
|                   | $E_{2u} \downarrow$ | $A_{1g} \downarrow$ | $E_{2u} \downarrow$ | $E_{1g} \downarrow$ | $B_{1u} \downarrow$ | $E_{1g} \downarrow$ |
| $E_{2u} \uparrow$ | $C_2$               | 0                   | 0                   | 0                   | $C_4$               | 0                   |
| $A_{1g} \uparrow$ | 0                   | 0                   | 0                   | $-C_3$              | 0                   | $-C_4$              |
| $E_{2u} \uparrow$ | 0                   | 0                   | $-C_2$              | 0                   | $C_3$               | 0                   |
| $E_{1g} \uparrow$ | 0                   | $C_4$               | 0                   | $C_2$               | 0                   | 0                   |
| $B_{1u} \uparrow$ | $-C_3$              | 0                   | $-C_4$              | 0                   | 0                   | 0                   |
| $E_{1g} \uparrow$ | 0                   | $C_3$               | 0                   | 0                   | 0                   | $-C_2$              |

(11)

|                   | $n=5$                | $n=0$                | $n=1$                | $n=2$                | $n=3$                | $n=4$                |
|-------------------|----------------------|----------------------|----------------------|----------------------|----------------------|----------------------|
|                   | $E_{2u} \uparrow$    | $A_{1g} \uparrow$    | $E_{2u} \uparrow$    | $E_{1g} \uparrow$    | $B_{1u} \uparrow$    | $E_{1g} \uparrow$    |
| $E_{2u} \uparrow$ | $\frac{\lambda}{6}$  | 0                    | $\frac{\lambda}{6}$  | 0                    | $-\frac{\lambda}{3}$ | 0                    |
| $A_{1g} \uparrow$ | 0                    | $\frac{\lambda}{6}$  | 0                    | $-\frac{\lambda}{3}$ | 0                    | $\frac{\lambda}{6}$  |
| $E_{2u} \uparrow$ | $\frac{\lambda}{6}$  | 0                    | $-\frac{\lambda}{3}$ | 0                    | $\frac{\lambda}{6}$  | 0                    |
| $E_{1g} \uparrow$ | 0                    | $-\frac{\lambda}{3}$ | 0                    | $\frac{\lambda}{6}$  | 0                    | $\frac{\lambda}{6}$  |
| $B_{1u} \uparrow$ | $-\frac{\lambda}{3}$ | 0                    | $\frac{\lambda}{6}$  | 0                    | $\frac{\lambda}{6}$  | 0                    |
| $E_{1g} \uparrow$ | 0                    | $\frac{\lambda}{6}$  | 0                    | $\frac{\lambda}{6}$  | 0                    | $-\frac{\lambda}{3}$ |

(12)

|                   | $n=5$                | $n=0$               | $n=1$                | $n=2$                | $n=3$               | $n=4$                |
|-------------------|----------------------|---------------------|----------------------|----------------------|---------------------|----------------------|
|                   | $E_{2u} \downarrow$  | $A_{1g} \downarrow$ | $E_{2u} \downarrow$  | $E_{1g} \downarrow$  | $B_{1u} \downarrow$ | $E_{1g} \downarrow$  |
| $E_{2u} \uparrow$ | $C_1 i$              | $C_5$               | 0                    | $-\frac{\lambda}{6}$ | $C_6$               | $C_7$                |
| $A_{1g} \uparrow$ | $C_5^*$              | 0                   | $C_5$                | $-C_6^*$             | $\frac{\lambda}{3}$ | $-C_6$               |
| $E_{2u} \uparrow$ | 0                    | $C_5^*$             | $-C_1 i$             | $C_7^*$              | $C_6^*$             | $-\frac{\lambda}{6}$ |
| $E_{1g} \uparrow$ | $-\frac{\lambda}{6}$ | $C_6$               | $C_7$                | $C_1 i$              | $C_5$               | 0                    |
| $B_{1u} \uparrow$ | $-C_6^*$             | $\frac{\lambda}{3}$ | $-C_6$               | $C_5^*$              | 0                   | $C_5$                |
| $E_{1g} \uparrow$ | $C_7^*$              | $C_6^*$             | $-\frac{\lambda}{6}$ | 0                    | $C_5^*$             | $-C_1 i$             |

(13)

with  $C_1 = \frac{\lambda}{\sqrt{12}}$ ,  $C_2 = \frac{\lambda}{\sqrt{12}}(1+i)$ ,  $C_3 = 0.105663\lambda(1+i)$ ,  $C_4 = 0.394337\lambda(1+i)$ ,  $C_5 = \frac{\lambda}{12} + \frac{\lambda}{2\sqrt{12}}i$ ,  $C_6 = \frac{\lambda}{4} + \frac{\lambda}{2\sqrt{12}}i$ ,  $C_7 = -\frac{\lambda}{6} + \frac{\lambda}{\sqrt{12}}i$ .

Several comments are in place here. First, spin-orbit coupling mixes QMOs at all  $\mathbf{k}$ -vectors. Even at the  $\Gamma$  point, *i. e.*, on the same hexagon, the three upper QMOs ( $A_{1g}$  and two  $E_{2u}$ ) are SO coupled to the three lower QMOs ( $B_{1u}$  and two  $E_{1g}$ ), which explains sizable shifts of the relativistic bands compared to the non-relativistic ones at this  $\mathbf{k}$ -vector. Additionally, SO coupling induces splitting of the degenerate  $E_{2u}$  and  $E_{1g}$  states at all  $\mathbf{k}$ -vectors. Another striking feature of the calculated  $\lambda \mathbf{L} \cdot \mathbf{S}$  matrix is that its  $A_{1g}$ ,  $E_{2u}$  (upper triplet) and  $B_{1u}$ ,  $E_{1g}$  (lower triplet) blocks are identical. This means that if not for the accidental near-degeneracy of the  $A_{1g}$  and  $E_{2u}$  states (which magnifies the SO induced energy shifts) the upper and the lower triplets would have been equally affected by the SO coupling.

## B. Quasimolecular orbital basis versus relativistic basis

The main difficulty in describing the  $\text{Na}_2\text{IrO}_3$  band-structure is that it interpolates between eigenstates of two Hamiltonians: the *itinerant* TB Hamiltonian of (primarily) *intra*hexagon electron hopping that preserves the  $s_z$  spin subspace and the *local* spin-orbit (SO) interaction  $\lambda \mathbf{L} \cdot \mathbf{S}$  Hamiltonian that couples *different* spin subspaces. The eigenstates of the TB Hamiltonian are quasimolecular orbitals (QMOs), while the eigenstates of the SO interaction (in the  $t_{2g}$  subspace) are *relativistic orbitals* (ROs)  $|j_{\text{eff}}, j_{\text{eff}}^z\rangle$  characterized by an effective total angular momentum  $j_{\text{eff}}$  and its  $z$ -projection  $j_{\text{eff}}^z$ :

$$\begin{aligned}
|\frac{1}{2}, \frac{1}{2}\rangle &= \frac{1}{\sqrt{3}}|xy \uparrow\rangle + \frac{i}{\sqrt{3}}|xz \downarrow\rangle + \frac{1}{\sqrt{3}}|yz \downarrow\rangle, \\
|\frac{1}{2}, -\frac{1}{2}\rangle &= \frac{i}{\sqrt{3}}|xz \uparrow\rangle - \frac{1}{\sqrt{3}}|yz \uparrow\rangle + \frac{1}{\sqrt{3}}|xy \downarrow\rangle, \\
|\frac{3}{2}, \frac{3}{2}\rangle &= \frac{i}{\sqrt{2}}|xz \uparrow\rangle + \frac{1}{\sqrt{2}}|yz \uparrow\rangle, \\
|\frac{3}{2}, \frac{1}{2}\rangle &= -\sqrt{\frac{2}{3}}|xy \uparrow\rangle + \frac{i}{\sqrt{6}}|xz \downarrow\rangle + \frac{1}{\sqrt{6}}|yz \downarrow\rangle, \\
|\frac{3}{2}, -\frac{1}{2}\rangle &= \frac{i}{\sqrt{6}}|xz \uparrow\rangle - \frac{1}{\sqrt{6}}|yz \uparrow\rangle - \sqrt{\frac{2}{3}}|xy \downarrow\rangle, \\
|\frac{3}{2}, -\frac{3}{2}\rangle &= -\frac{i}{\sqrt{2}}|xz \downarrow\rangle + \frac{1}{\sqrt{2}}|yz \downarrow\rangle.
\end{aligned} \quad (14)$$

This basis<sup>23</sup> can be explained as follows; three  $t_{2g}$  orbitals (total degeneracy, including spins, is 6) are split into a lower-lying quartet  $j_{\text{eff}} = 3/2$  and an upper-lying  $j_{\text{eff}} = 1/2$  doublet, and the 5d-electrons of  $\text{Ir}^{4+}$  fully occupy the lower quartet leaving the upper  $j_{\text{eff}} = 1/2$  doublet half-filled. This makes this situation similar to a non-degenerate Hubbard model ( $S=1/2$  doublet on a site), with the important difference that in the Hubbard model the hopping matrix elements preserve the  $s_z$  spin subspace, while here the states of the  $j_{\text{eff}} = 1/2$  doublet are spin-orbit mixed states, leading to a strong anisotropy of hoppings and their dependence on spin (or rather total moment) direction. This may bring about anisotropic exchange, *e. g.*, the Kitaev exchange on a honeycomb lattice<sup>2</sup>.

By gradually increasing an effective spin-orbit coupling strength  $\lambda_{\text{eff}}$ ,

$$\lambda_{\text{eff}} = \frac{\lambda^2}{(t_{10})^2 + \lambda^2}, \quad t_{10} = 0.270 \text{ eV}, \quad (15)$$

from 0 to 1, one can trace a smooth evolution of the TB+SO model eigenvalues from, respectively, the non-relativistic (QMO) limit to the fully relativistic (RO) limit (see Fig. 8 (a) for the data at the  $\Gamma$  point). An SO coupling parameter of  $\lambda = 0.44$  eV for  $\text{Na}_2\text{IrO}_3$  corresponds to  $\lambda_{\text{eff}} = 0.73$ , which is marked by a vertical dotted line in Fig. 8.

The RO basis is an attractive starting point to describe the low-energy physics of  $\text{Na}_2\text{IrO}_3$  as it allows to truncate the Hamiltonian to only  $j_{\text{eff}} = \frac{1}{2}$  states that dominate near the Fermi energy and map  $\text{Na}_2\text{IrO}_3$  onto the Kitaev-Heisenberg model. Although this approach might seem reasonable given the noticeable separation of the  $j_{\text{eff}} = \frac{1}{2}$  and  $j_{\text{eff}} = \frac{3}{2}$  characters in the DOS of  $\text{Na}_2\text{IrO}_3$  [*cf.* Fig. 2 (b) of Ref. 22], we argue that the itinerant terms are too strong to be neglected (which should not be surprising since  $\lambda = 0.44 \text{ eV} < W \approx 4t_{10} = 1 \text{ eV}$ ) and that, consequently, the QMO basis is as well (or as poorly) justified to work with as the RO basis.

To support this statement, let us concentrate on the TB+SO model states at the  $\Gamma$  point. Fig. 8 (a) shows the evolution of the model eigenvalues as a function of  $\lambda_{\text{eff}}$  (Eq. 15). In the non-relativistic limit ( $\lambda_{\text{eff}} = 0$ ), the states are almost purely (with slight deviation due to orthorhombic distortion) QMOs, ordered as  $B_{1u}, E_{1g}, A_{1g}, E_{2u}$  with increasing energy<sup>24</sup>. At the same time, at each state the  $j_{\text{eff}} = \frac{1}{2}$  contribution is 1/3 and the  $j_{\text{eff}} = \frac{3}{2}$  contribution is, correspondingly, 2/3 (for one of the two Ir atoms). Note that, since the model distinguishes spin- $\uparrow$  and spin- $\downarrow$  states each level is doubly degenerate.

With the QMO splitting obviously prevailing for zero SO coupling, we now want to quantify the QMO character rectification upon increasing  $\lambda_{\text{eff}}$  by calculating the QMO and RO weights on two selected states: the lowest ( $B_{1u}$ ) and the uppermost ( $E_{2u}$ ). The  $B_{1u}$  state [Fig. 8 (b)] is a simpler case as it is non-degenerate (apart from spin) and quite well separated from the rest of the

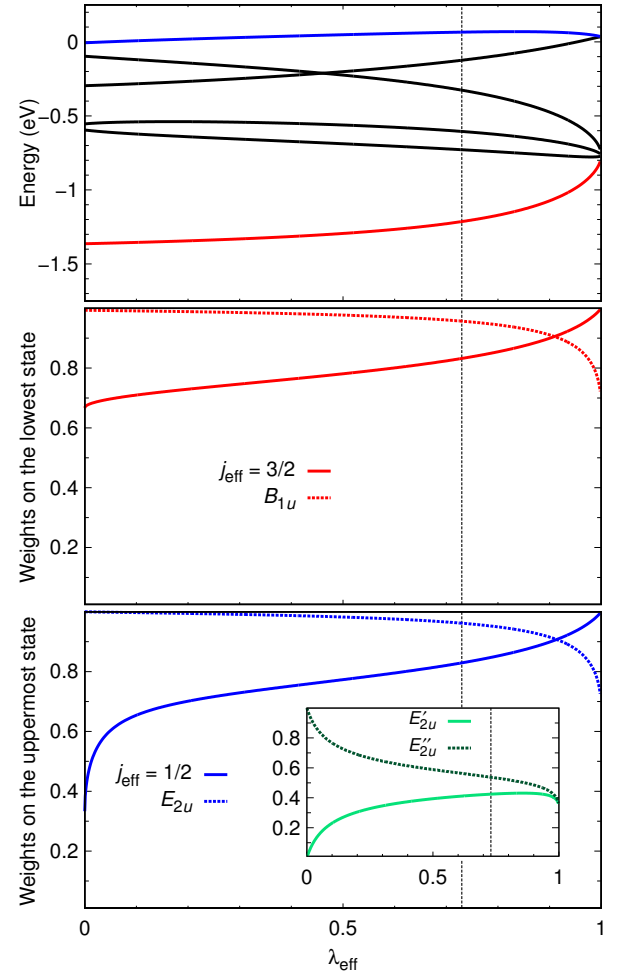


FIG. 8: Properties of the TB+SO model of  $\text{Na}_2\text{IrO}_3$  at the  $\Gamma$  point as a function of effective SO coupling  $\lambda_{\text{eff}}$  defined in Eq. (15). The vertical dotted line marks the realistic  $\lambda_{\text{eff}} = 0.73$  value for  $\text{Na}_2\text{IrO}_3$ . (a) The eigenvalues of the TB+SO model at  $\Gamma$ . Eigenenergies have been scaled by  $\sqrt{1 - \lambda_{\text{eff}}}$  to keep them within the  $[-1.5, 0.2]$  eV range. (b) The  $j_{\text{eff}} = \frac{3}{2}$  (solid line) and  $B_{1u}$  (dashed line) weights on the lowest state. (c) The  $j_{\text{eff}} = \frac{1}{2}$  (solid line) and total  $E_{2u}$  (dashed line) weights on the uppermost state. Inset shows individual contributions from the two  $E_{2u}$  QMOs.

QMOs so that the SO effects here should be less important. Changing  $\lambda_{\text{eff}}$  from 0 to 0.73 ( $\text{Na}_2\text{IrO}_3$  value), the  $j_{\text{eff}} = \frac{3}{2}$  weight on this state increases from 0.6667 to 0.8320, whereas the  $B_{1u}$  weight is only slightly reduced from 0.9932 to 0.9567. This indicates that the lowest relativistic state at the  $\Gamma$  point in  $\text{Na}_2\text{IrO}_3$  is better described by a QMO  $B_{1u}$  than by one of the  $j_{\text{eff}} = \frac{3}{2}$  ROs. In fact, this turns out to hold for the whole lowest relativistic band [*cf.* the  $j_{\text{eff}}$ - and QMO-projected  $\text{Na}_2\text{IrO}_3$  DOS in, respectively, Fig. 2 (b) of Ref. 22 and Fig. S6 (b) of Ref. 5].

The uppermost state is one of the  $E_{2u}$  doublet states. It is near-degenerate with  $A_{1g}$  and the other  $E_{2u}$  and, therefore, the SO effects are here particularly strong. At

the  $\Gamma$  point, though, it can only couple to itself or to the other  $E_{2u}$  [see Eqs. (10) and (11)], depending on which linear combination of these degenerate states is considered. Upon switching  $\lambda_{\text{eff}}$  on, the  $j_{\text{eff}} = \frac{1}{2}$  weight on this upper states rapidly grows from 0.3333 to  $\sim 0.6$  in the range  $0 < \lambda_{\text{eff}} < 0.05$ , and then gradually increases to 0.8295 at  $\lambda_{\text{eff}} = 0.73$  [Fig. 8 (c)]. At the same time, the weight of one of the  $E_{2u}$  states (we may call it  $E'_{2u}$ ) is reduced from 1.0 to 0.53730 [see inset of Fig. 8 (c)]. However, the total weight of two  $E_{2u}$  states is barely changed: at  $\lambda_{\text{eff}} = 0.73$  it equals 0.9617. This means that the uppermost relativistic state at the  $\Gamma$  point in  $\text{Na}_2\text{IrO}_3$  is very well described by a linear combination of two  $E_{2u}$  states (which is also a QMO) with, in general,  $\lambda_{\text{eff}}$ -dependent individual contributions.

The  $B_{1u}$  and  $E_{2u}$  states (at  $\lambda = 0$ ) seem to simultaneously bear both RO and QMO features up to very strong SO coupling, with the QMO character dominating for  $\lambda_{\text{eff}} < 0.9$ . This can also be illustrated by inspecting the composition of, *e. g.*, the lowest energy band state as shown in Table III. At zero SO coupling, the doubly degenerate lowest state corresponds to (almost) pure  $B_{1u} \uparrow$  and  $B_{1u} \downarrow$  QMOs<sup>25</sup>. At  $\lambda_{\text{eff}} = 0.73$ , the structure of this state is strikingly similar to the  $B_{1u}$  states, with only slight admixtures of the  $xz$  and  $yz$  orbitals of opposite spin. Even at some very high  $\lambda_{\text{eff}}$ , when the RO  $j_{\text{eff}} = \frac{3}{2}$  weight is close to 1, the states retain the  $B_{1u} \uparrow$  and  $B_{1u} \downarrow$  QMO features.

The features shown in this Section, not unexpectedly, characterize  $\text{Na}_2\text{IrO}_3$  as intermediate between the non-relativistic (pure quasi-molecular orbital) and fully relativistic (pure RO) cases.

Moreover, these results show that, in the RO representation, the upper band states are not pure  $j_{\text{eff}} = 1/2$  states but there is some significant mixing of  $j_{\text{eff}} = 3/2$  states. In fact, for the upper band states, the projections onto  $j_{\text{eff}} = 1/2$  and  $j_{\text{eff}} = 3/2$  are, respectively, 0.64 and 0.21 with  $2(0.64^2 + 2 \times 0.21^2) = 1$ , while in the non-relativistic case these projections are both equal to  $\sqrt{1/6} = 0.41$ . Note that looking at the weights may be misleading. Indeed this state appears to be  $2 \times 0.64^2 = 82\%$  pure  $j_{\text{eff}} = 1/2$  state [Fig. 8 (bottom)], but its *projection* on the  $j_{\text{eff}} = 3/2$  state is only twice smaller than in the non-relativistic case. In other words, the hopping between the upper Kramers doublets, initially not considered in Ref. 2, is only reduced by about a factor of two compared to the non-relativistic case. One but possibly not the only consequence of this fact is that the contribution of the Kitaev term in the analysis below may be overestimated, probably by as much as a factor of two.

### C. Comparison with experiment: branching ratio

An argument frequently used to justify the assumption of pure ROs in  $\text{Na}_2\text{IrO}_3$  is that it is experimentally supported. However, the experimental evidence is incon-

clusive. It is first assumed that the electronic states are pure ROs and then it is shown that this assumption does not contradict the experiment, yet the experiments, upon a closer look, do not falsify the DFT picture, either. A typical and, by far, the most often used quantity to discuss the nature of the states in iridates is the branching ratio (BR) extracted from X-ray absorption spectroscopy (XAS) experiments. In XAS, essentially,  $\langle \mathbf{L} \cdot \mathbf{S} \rangle$  is measured. This expectation value is of course zero without spin-orbit coupling. A detailed and very insightful analysis can be found, for instance, in Refs. 26–29. In particular, it is shown that, for a related iridate, the main contribution to  $\langle \mathbf{L} \cdot \mathbf{S} \rangle$  (1.4 out of 2.1) doesn't come from the  $t_{2g}$  orbitals, which define the  $j_{\text{eff}} = 1/2$  states, but from the admixture of the  $e_g$  orbitals. In our calculations –shown below– we observe the same behavior.

We apply our TB+SO model to calculate  $\langle \mathbf{L} \cdot \mathbf{S} \rangle$  for  $\text{Na}_2\text{IrO}_3$  where  $\mathbf{L}$  and  $\mathbf{S}$  are, respectively, the *total* orbital and spin angular momenta of Ir 5d electrons.  $\langle \mathbf{L} \cdot \mathbf{S} \rangle$  is related to the experimentally accessible branching ratio as

$$\text{BR} = \frac{(2-r)}{(1+r)}, \quad r = \frac{\langle \mathbf{L} \cdot \mathbf{S} \rangle}{n_h}, \quad (16)$$

with  $n_h = 5$  being the average number of 5d Ir holes<sup>30,31</sup>. In recent XAS measurements<sup>32</sup>,  $\text{BR} = 5.5 - 5.7$ , translating to  $\langle \mathbf{L} \cdot \mathbf{S} \rangle = -2.7\hbar^2$ , was obtained for  $\text{Na}_2\text{IrO}_3$  and interpreted as a sign of strong spin-orbit coupling.

When applying the TB+SO model that we constructed for  $\text{Na}_2\text{IrO}_3$  in Section V A the calculated  $\langle \mathbf{L} \cdot \mathbf{S} \rangle = -0.73\hbar^2$  (as compared to  $-1\hbar^2$  in the limit  $\lambda_{\text{eff}} = 1$ ). This value is several times smaller than the experimental value. This is, however, not unexpected given the significant contribution of the Ir  $e_g$  empty states to  $\langle \mathbf{L} \cdot \mathbf{S} \rangle$  (*cf.* Ref. 26), which are not considered in the TB+SO model discussed in the previous Section. In order to make a meaningful comparison with experiment, we extend our TB+SO model to include (in the same spirit) also the Ir  $e_g$  states.  $\langle \mathbf{L} \cdot \mathbf{S} \rangle$  within such a model is  $-1.91\hbar^2$ . This is about 30% less than the experimental value reported by Clancy *et al.*<sup>32</sup>. This result is indeed in good agreement with experiment, given the large fluctuations in experimental values. For instance, Ref. 32 reported  $\langle \mathbf{L} \cdot \mathbf{S} \rangle = -3.1\hbar^2$  for  $\text{Sr}_2\text{IrO}_4$  while Ref. 26 reported  $-2.1\hbar^2$  (about 30% difference) for the same compound. This example gives a sense of possible fluctuations between results of different experimental groups, and therefore our theoretical  $\langle \mathbf{L} \cdot \mathbf{S} \rangle$  value for  $\text{Na}_2\text{IrO}_3$  might be even closer to the true result.

The main conclusion from these calculations is that with the TB+SO model based on all *five* Ir 5d orbitals we are able to reasonably reproduce the large experimentally measured  $\langle \mathbf{L} \cdot \mathbf{S} \rangle$  value in  $\text{Na}_2\text{IrO}_3$ , which validates our approach. As our analysis shows, the large  $\langle \mathbf{L} \cdot \mathbf{S} \rangle$  does not necessarily mean an ideal separation of  $j_{\text{eff}} = \frac{3}{2}$  and  $j_{\text{eff}} = \frac{1}{2}$  RO states, but rather the effect of  $e_g$  states also contributing in the process. Due to the peculiar electron hopping hierarchy in  $\text{Na}_2\text{IrO}_3$ , QMOs might be a better

TABLE III: Expansion coefficients of the lowest doubly degenerate energy states of the TB+SO model in the  $t_{2g}$  basis (The upper index of the  $t_{2g}$  orbitals labels Ir atoms in the unit cell). The coefficients are given for three  $\lambda$  ( $\lambda_{\text{eff}}$ ) values. The  $B_{1u}$  and  $j_{\text{eff}} = \frac{3}{2}$  weights of the various states are given at the bottom of the table.

|                                       | $\lambda = 0$ ( $\lambda_{\text{eff}} = 0$ ) |        | $\lambda = 0.44$ eV ( $\lambda_{\text{eff}} = 0.73$ ) |                   | $\lambda = 2.66$ eV ( $\lambda_{\text{eff}} = 0.99$ ) |                   |
|---------------------------------------|--|--------|---|-------------------|---|-------------------|
| $xy^1 \uparrow$                       | -0.454                                       | 0.0    | -0.453  | 0.0               | -0.444  | 0.0               |
| $xz^1 \uparrow$                       | -0.383                                       | 0.0    | $-0.363 + 0.056i$                                     | $-0.053 - 0.100i$ | $-0.263 + 0.150i$                                     | $-0.142 - 0.200i$ |
| $yz^1 \uparrow$                       | -0.383                                       | 0.0    | $-0.363 - 0.056i$                                     | $-0.100 - 0.053i$ | $-0.263 - 0.150i$                                     | $-0.200 - 0.142i$ |
| $xy^2 \uparrow$                       | 0.454  | 0.0    | 0.453   | 0.0               | 0.444   | 0.0               |
| $xz^2 \uparrow$                       | 0.383  | 0.0    | $0.363 - 0.056i$                                      | $0.053 + 0.100i$  | $0.263 - 0.150i$                                      | $0.142 + 0.200i$  |
| $yz^2 \uparrow$                       | 0.383  | 0.0    | $0.363 + 0.056i$                                      | $0.100 + 0.053i$  | $0.263 + 0.150i$                                      | $0.200 + 0.142i$  |
| $xy^1 \downarrow$                     | 0.0  | -0.454 | 0.0   | -0.453            | 0.0   | -0.444            |
| $xz^1 \downarrow$                     | 0.0  | -0.383 | $0.053 - 0.100i$                                      | $-0.363 - 0.056i$ | $0.142 - 0.200i$                                      | $-0.263 - 0.150i$ |
| $yz^1 \downarrow$                     | 0.0  | -0.383 | $0.100 - 0.053i$                                      | $-0.363 + 0.056i$ | $0.200 - 0.142i$                                      | $-0.263 + 0.150i$ |
| $xy^2 \downarrow$                     | 0.0  | 0.454  | 0.0   | 0.453             | 0.0   | 0.444             |
| $xz^2 \downarrow$                     | 0.0  | 0.383  | $-0.053 + 0.100i$                                     | $0.363 + 0.056i$  | $-0.142 + 0.200i$                                     | $0.263 + 0.150i$  |
| $yz^2 \downarrow$                     | 0.0  | 0.383  | $-0.100 + 0.053i$                                     | $0.363 - 0.056i$  | $-0.200 + 0.142i$                                     | $0.263 - 0.150i$  |
| $j_{\text{eff}} = \frac{3}{2}$ weight | 0.6667                                       |        | 0.8320  |                   | 0.9816  |                   |
| $B_{1u}$ weight                       | 0.9932                                       |        | 0.9567  |                   | 0.7824  |                   |

basis.

In conclusion, the XAS experiments only tell us that the upper Kramers doublet has a considerable contribution coming from  $j_{\text{eff}} = 1/2$ , but not that it is a pure RO state.

#### D. Comparison with experiment: RIXS

Another experiment sometimes quoted as supporting the fully relativistic  $j_{\text{eff}} = \frac{1}{2}$  picture is resonant inelastic x-ray scattering (RIXS)<sup>33</sup>. In this experiment a joint density of electronic states (JDOS) is probed, somewhat similar to that in the infrared absorption but with different matrix elements. The authors of Ref. 33 observed several peaks in JDOS, of which the lowest peak at  $\sim 0.42$  eV was interpreted as transitions across the Mott-Hubbard gap, consistent with a 30% smaller optical absorption threshold. The next two peaks are close to each other at 0.72 and 0.83 eV and were ascribed to transitions from the  $j_{\text{eff}} = 3/2$  quartet into the upper  $j_{\text{eff}} = 1/2$  doublet. The splitting of 110 meV was ascribed to the trigonal splitting. Altogether, this interpretation suggests an SO coupling  $\lambda \sim \frac{2}{3}(\frac{0.72+0.83}{2} - \frac{0.42}{2})\text{eV} \approx 0.39\text{eV}$ , a very reasonable number, if slightly too small.

This analysis, even though it looks reasonable on the first glance, has serious shortcomings. First, the deduced trigonal splitting is nearly twice as large as the actual trigonal splitting. In fact, the trigonal splitting is decided by the electrostatic field of the ligands, and in addition one-electron hoppings; both are very well accounted for by the DFT calculations, which give  $\Delta_T = 75$  meV. Second, even a  $\Delta_T = 110$  meV cannot produce well separated peaks in JDOS, given that the Ir-Ir hopping is  $t_{1O} = 270$  meV. Third, even if one completely neglects the Ir-Ir hoppings<sup>33</sup>, in order to extract  $\lambda$  and

$\Delta_T$  one has to diagonalize the full Hamiltonian including both factors and then fit the resulting eigenvalues to the observed peaks. After doing that, one gets  $\lambda = 0.5$  eV and  $\Delta_T = 180$  meV. Although the previous numbers are a rough estimate since they depend on the direction of the Ir spins as well as on  $U$  (here we considered  $U = 0$ ), the latter number is more than twice the actual trigonal splitting. This argument shows that an interpretation of RIXS in terms of infinitely narrow bands split by the trigonal field may not be completely correct.

We find, on the other hand, that this experiment is consistent with DFT band structure. To demonstrate that, we have performed DFT calculations for the magnetic zigzag phase. We note that the results do not depend qualitatively on the choice of the pattern and the magnetization direction. In order to account for the missing correlation effects and adjust the direct gap to be consistent with infrared measurements<sup>11</sup>, we applied a rigid shift of 200 meV between the occupied and empty bands (“scissor operator”). This exercise gives a JDOS which has a broad feature, consisting of (i) a peak at 0.42 and a shoulder 0.48 eV (compared to 0.42 eV in the experiment) corresponding to the transition between the top QMOs and (ii) a peak at 0.77 eV and a shoulder at 0.81 eV corresponding to transitions from the lower QMOs. While the experiment finds two peaks at 0.72 and 0.83 eV, one should keep in mind that the matrix elements, omitted in our calculation, can easily suppress or enhance a shoulder, making it disappear (at 0.48 eV) or become a separate peak (at 0.81 eV). Therefore we conclude that the agreement between experiment and our calculations, simplified as they are, is reasonably good.

## VI. MAGNETISM

We proceed now with the discussion of the magnetic behavior of  $\text{Na}_2\text{IrO}_3$ . Neutron diffraction experiments reported long-range antiferromagnetic order at low temperatures in a zigzag pattern<sup>8</sup>. This ordering was confirmed by relativistic spin-polarized DFT calculations<sup>5</sup> where we showed that it is the itinerancy of the system that stabilizes the zigzag configuration. Such a pattern was also predicted from the localized nnKH model<sup>2,4</sup> (Eq. 1). In the following we will provide *ab initio*-derived estimates for the Kitaev and Heisenberg terms and will show that in the physically reasonable parameter range this model unfortunately fails to reproduce the experimentally observed magnetic order.

### A. Nearest neighbor Kitaev-Heisenberg model

One term neglected in the conventional Kitaev-Heisenberg model treatment is the single-site magnetocrystalline anisotropy. Localized electrons with the spin 1/2 do not have any anisotropy, no matter how strong the spin-orbit coupling is. However, if hopping is considered, electrons can have a preferred spin direction, which in the language of the nnKH Hamiltonian would be reflected in a single-site term proportional, in the lowest order, to  $(\mathbf{A} \cdot \mathbf{S})^2$  where  $\mathbf{A}$  is a vector. Such terms are usually neglected when dealing with the nnKH model. Our calculations<sup>5</sup> without including  $U$  show a magnetic anisotropy as large as 3 meV per Ir (in order to address the single-site anisotropy, we compared ferromagnetic calculations). This energy should be compared to the total magnetic stabilization energy (i.e. the energy difference between magnetic and non-magnetic solutions) of maximally 5 meV. When the DFT calculations are performed including a  $U = 2$  eV, the magnetic anisotropy is as large as 8 meV out of a total energy of 28 meV. This substantial anisotropy suggests that a single site term should be added to the Kitaev-Heisenberg Hamiltonian, probably resulting in a rather different phase diagram.

With all these caveats, it is still instructive to analyze where  $\text{Na}_2\text{IrO}_3$  is to be found in the parametric space of the nnKH model. We make the following assumptions: (i) that the atomic orbitals are fully localized and the appropriate basis is given by pure  $j_{\text{eff}} = 1/2$  orbitals; (ii) that the only hoppings relevant for magnetic interactions are  $pd$  hoppings, so that the only oxygen assisted Ir-Ir hoppings are specific  $t_{2g} - t_{2g}$  hoppings between unlike orbitals, as outlined in Refs. 2,5, and the  $t_{2g} - e_g$  hoppings given in Ref. 4; and (iii) that the only processes contributing to magnetic interactions are those listed in Ref. 4.

Indeed, the fact that the experimentally observed magnetic order is zigzag suggests that either the Heisenberg terms are exceptionally long ranged (the 3rd neighbor exchange is comparable to the 1st one)<sup>7,8</sup>, or that the Kitaev term is strong and antiferromagnetic<sup>4,34</sup>. The for-

mer suggestion is seemingly in contradiction with the fact that the calculated 3rd neighbor hoppings are substantially smaller than the 1st neighbor ones. This makes it impossible to explain the large 3rd neighbor exchange integral in terms of superexchange. However, there is a possibility, suggested in Ref. 5, that the Ir electrons are itinerant over individual hexagons, which makes magnetic interactions naturally long ranged, and not directly related to the hopping integrals.

The second suggestion, which is the one we will focus on in what follows, was proposed in Ref. 4, namely that of an antiferromagnetic Kitaev term. If strong enough, this could explain the observed magnetic order. Below we consider the expressions presented in Ref. 4 and substitute the unknown variables with *ab initio*-derived parameters.

Chaloupka *et al.*<sup>4</sup> discuss four relevant processes contributing to the exchange interactions in  $\text{Na}_2\text{IrO}_3$ : (1) Direct hopping  $t_{1\sigma}$  between nearest neighbor Ir  $t_{2g}$  orbitals contributing with a term  $I_1 = (\frac{2}{3}t_{1\sigma})^2/U$  to the Heisenberg term, where  $U$  is the Coulomb repulsion between  $t_{2g}$  electrons.

(2) Interorbital nearest neighbor Ir  $t_{2g}-e_g$  hopping via intermediate oxygens  $\tilde{t}_1$ , with  $\tilde{t}_1 = t_{pd\sigma}t_{pd\pi}/\Delta$ , where  $\Delta$  is the charge-transfer energy (the difference between the O  $p$  and Ir  $d$  levels) contributing with a term  $I_2 = \frac{4}{9}\frac{\tilde{t}_1^2}{U}\frac{\tilde{J}_H}{U}$  both to the Kitaev and Heisenberg terms, but with the opposite signs. Here  $\tilde{U}$  is the excitation energy associated with the  $t_{2g}-e_g$  hopping *i.e.* it also includes crystal field splitting,  $\tilde{U} = U + 10Dq$ .  $\tilde{J}_H$  is the Hund's rule coupling between  $t_{2g}$  and  $e_g$  electrons.

(3) Oxygen-assisted hopping between two nearest neighbor Ir  $t_{2g}$  orbitals  $t_{1O}$  contributing with a term  $I_3 = \frac{8}{3}\frac{t_{1O}^2}{U}\frac{J_H}{U}$  to the Kitaev term, where  $J_H$  is the Hund's rule coupling between  $t_{2g}$  electrons, and, we remind,  $t_{1O} = t_{pd\pi}^2/\Delta$ .

(4) Oxygen-2p – Iridium-5d charge transfer contributing with a term  $I_4 = \frac{8t_{1O}^2}{9}\left[\frac{1}{2\Delta+U_p-3J_p} + \frac{1}{3(2\Delta+U_p-J_p)} + \frac{2}{3(2\Delta+U_p+2J_p)} - \frac{1}{\Delta}\right]$ , where  $U_p$  and  $J_p$  are, respectively, the Hubbard repulsion and the Hund's rule parameter for oxygen. This expression was derived by G. Khaliullin<sup>35</sup> and is worth some additional discussion. The first three terms correspond to processes where two holes of the same or of opposite spins meet at an oxygen atom. Neglecting  $J_p$ , one gets simply  $\frac{8t_{1O}^2}{9}\frac{1}{\Delta+U_p/2}$ , which reflects the fact that if the Ir atoms have opposite spins one can create an intermediate state with two holes on the same oxygen orbital, which lowers the total energy. The last term appears due to ring exchange, with an intermediate state where two holes are located on different oxygens. This process is only allowed when the ground state is FM, and only if the ground state hole is in an  $a_{1g}$  or  $j_{\text{eff}} = 1/2$  state, but not for pure  $t_{2g}$  orbitals. However, contrary to a common misconception,  $J_p$  is large, between 1.2 and 1.6 eV. We have estimated  $U_p$  and  $J_p$ , using the technique described in Ref. 37, and obtained



| parameter      | value (eV) | meaning   |
|----------------|------------|---|
| $t_{1\sigma}$  | 0.03       | direct Ir-Ir hopping  |
| $t_{1O}$       | 0.27       | O assisted Ir-Ir hopping                                      |
| $\tilde{t}_1$  | 0.38       | Ir $t_{2g} - e_g$ hopping                                     |
| $t_{pd\pi}$    | 0.57*      | Ir-O $\pi$ hopping  |
| $t_{pd\sigma}$ | 1.6*       | Ir-O $\sigma$ hopping   |
| $\Delta$       | 2.4        | charge transfer energy<br>between the O $p$ and Ir $d$ levels |
| $J_H$          | 0.5        | Ir $t_{2g}$ Hund's rule coupling                              |
| $\tilde{J}_H$  | 0.5        | Ir $t_{2g} - e_g$ Hund's rule coupling                        |

TABLE IV: DFT-calculated values of transfer integrals and charge transfer energy for  $\text{Na}_2\text{IrO}_3$  and estimates of Hund's rule coupling strength as described in the text. The values marked with \* were obtained from  $\tilde{t}_1$ ,  $t_{1O}$  and  $\Delta$ .

$U_p = 2.7$  and  $J_p = 1.6$  eV, consistent with earlier DFT estimates<sup>36</sup>. For non-relativistic orbitals it is comparatively straightforward to account for the Hund's rule coupling on O, but for relativistic orbitals it becomes more tedious.

If we expand  $I_4$  in both  $U_p$  and  $J_p$ , then  $I_4 \approx \frac{8t_{1O}^2}{9} \frac{U_p - J_p}{2\Delta^2}$ . This expression shows that  $U_p$  alone contributes ferromagnetically to the Heisenberg term and antiferromagnetically to the Kitaev term and may shift the various phases in the nnKH model. Together with  $J_p$  though, for the values suggested above the effect of  $U_p$  and  $J_p$  largely cancels and  $I_4$  appears to be unimportant (note though that if  $J_p$  is entirely neglected, as in Ref. 4, this proposition becomes more questionable).

Summarizing the above terms into a single expression, Eq. (1) can be written as:

$$H_{ij}^{(\gamma)} = \underbrace{(2I_2 - I_3 + 2I_4)}_{2K} S_i^\gamma S_j^\gamma + \underbrace{(I_1 - I_2 - I_4)}_J \mathbf{S}_i \cdot \mathbf{S}_j. \quad (17)$$

This model has a zigzag magnetic ground state<sup>4</sup> if the Kitaev term is antiferromagnetic (AFM) and the Heisenberg term is ferromagnetic (FM), with  $K > 0$ ,  $J < 0$  and  $-26 \lesssim J/K \lesssim -0.3$ .

In Table IV we provide the parameter values relevant for  $\text{Na}_2\text{IrO}_3$ , as obtained from our DFT results. Note that the  $\tilde{t}_1$  parameter was assumed to be  $2t_{1O}$  in Ref. 4, while in the calculations (DFT calculations are usually very reliable in this respect)  $\tilde{t}_1/t_{1O}$  is 1.4. However, using the ratio of 2 hardly changes any conclusions.

We present our results in Figures 9 and 10. In Fig. 9 we show the calculated values of  $K$  and  $J$  as a function of two variables: the  $x$  axis is the Hubbard  $U$  associated with the upper Kramers doublet, and the  $y$  axis is the energy  $\tilde{U}$ , associated with exciting an individual electron from the upper  $t_{2g}$  to an average  $e_g$  state. The Hubbard  $U$  for 5d electrons is, generally speaking, 1.5 to 2 eV. However, in this case it is additionally screened by the  $e_g$  electrons, and also reduced by hybridization (cf.  $\text{Na}_x\text{CoO}_2$ <sup>38</sup> and Fe pnictides<sup>39</sup>). Experimental estimates of the Hubbard  $U$  defined as the energy cost for excit-

ing electrons across the insulating gap (which is the definition relevant to superexchange) yield 0.3-0.5 eV<sup>11,33</sup>. Additionally, LDA+U calculations with  $U \sim 2$  eV yield an excitation gap of the same order. We conclude that the realistic range of this parameter is 0.5–2 eV, with the smaller values more likely.

For the second parameter,  $\tilde{U}$ , DFT calculations give  $\sim 2.5$  eV. This should be considered as a lower bound since DFT tends to slightly overestimate the orbital overlap and crystal fields, and misses the effects of the  $t_{2g} - e_g$  Hubbard interaction. One can thus limit the physically admissible range in the region  $2.5 \text{ eV} \lesssim \tilde{U} \lesssim 3 \text{ eV}$ .

In Figure 10 we show the phase diagram in the space of the two parameters above. Several observations are in place: (1) While there is a zigzag phase in this diagram, it is very far removed from the range of the parameters that can be called physical,  $0.5 \text{ eV} \lesssim U \lesssim 2 \text{ eV}$ ,  $2 \text{ eV} \lesssim \tilde{U} \lesssim 3 \text{ eV}$  (even though in the above estimate we have liberally stretched the admissible range in favor of a zigzag phase). In fact, the zigzag regime appears only when  $\tilde{U} < 0.6U$ , i.e. when the Hubbard gap is larger than the  $e_g - t_{2g}$  splitting, a rather unlikely proposition. (2) In the physical range of parameters, the ground state is either ferromagnetic or the spin liquid phase. It is rather curious that the very narrow slivers of the phase space in the  $J, K$  coordinates<sup>4</sup> are transformed into a very large range in the  $U, \tilde{U}$  space.

It is also worth mentioning that in order to explain the experimental data of Refs. 7,8 one needs not only the ground state to be zigzag, but also that  $K$  be several times larger than  $|J|$ ; Chaloupka *et al.*<sup>4</sup> used  $K = 10.44$  and  $J = -4.01$  meV. This solution cannot be obtained for a given set of  $U$  and  $\tilde{U}$  (see Fig. 9). Moreover, a closer look at the expressions in their work reveals that  $K + J = I_1 - I_3/2$ , which does not depend on  $\tilde{U}$  and is always negative. Thus the two equalities above cannot be satisfied simultaneously for any choice of parameters, be they physical or not. Moreover, the values of  $J$  and  $K$  used in Ref. 4 can only be obtained if  $\tilde{U} < 0.2 \text{ eV}$ , which is clearly an impossible regime.

## B. Long-range exchange

As mentioned above, an alternative interpretation of the experimental results, given in Refs. 7,8, is in terms of sizable 2nd and 3rd neighbor exchange constants, comparable to the nearest neighbor exchange. In this picture the Kitaev term may or may not play a role, but this role is not decisive in establishing the observed magnetic order. Given that the calculated hopping amplitudes (Table I) are clearly dominated by the nearest neighbor terms, standard superexchange cannot explain such long range interactions.

However, it is important to remember that in the opposite, itinerant limit every electron is fully delocalized over a hexagon and, as such, is equally sensitive to the mean field magnetization pattern on the 1st, 2nd or 3rd

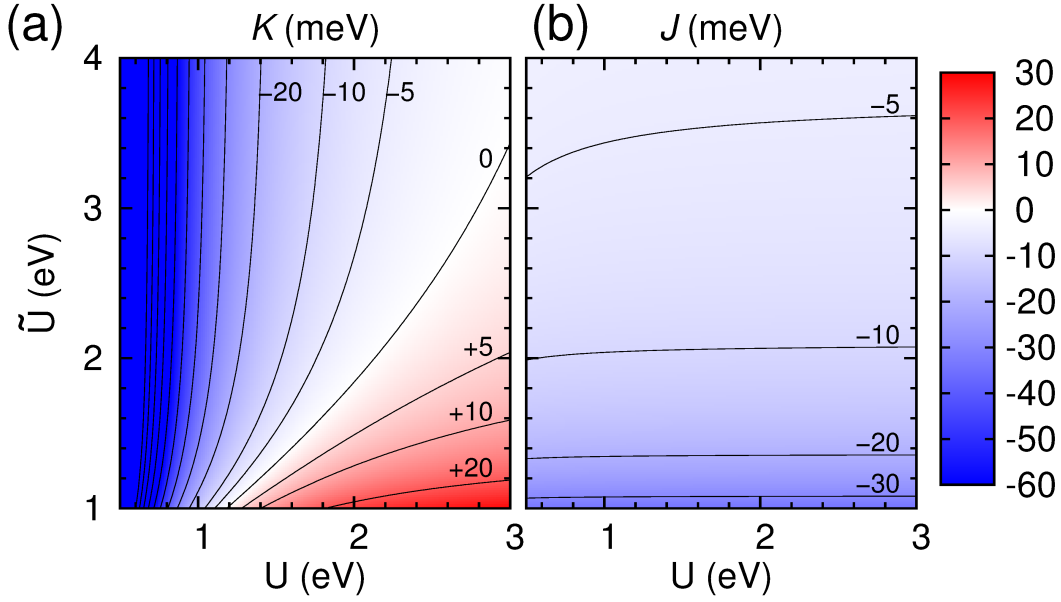
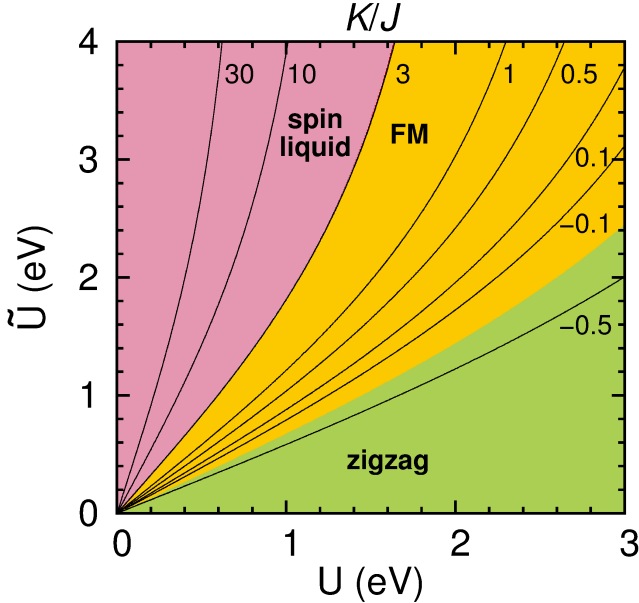


FIG. 9: (Color online) Variation of (a) Kitaev parameter  $K$  and (b) Heisenberg exchange coupling  $J$  with onsite Coulomb coupling strength  $U$  and Ir  $t_{2g}$ - $e_g$  excitation energy  $\tilde{U}$ . Positive values refer to antiferromagnetic, negative to ferromagnetic values of  $K$  and  $J$ . The other parameters entering the  $K$  and  $J$  are given in Table IV.

FIG. 10: (Color online) Phase diagram of the Kitaev-Heisenberg model for  $\text{Na}_2\text{IrO}_3$  with parameters determined following Ref. 4. The calculated exchange integrals are functions of the Mott-Hubbard gap  $U$  and the cubic crystal field splitting  $\tilde{U}$ . The contours mark isolines of the ratio  $K/J$ .



nearest neighbors. As discussed in our earlier work<sup>5</sup>, the zigzag order, as compared to the stripy one, results in a sizable pseudogap at the Fermi level even without a Hubbard  $U$ . This creates an energy gain that cannot be cast in a form of nearest neighbor interaction, as it depends

on the magnetization pattern over an entire hexagon.

We are far from stating that the superexchange Hamiltonian outlined in Ref. 4 is irrelevant and an itinerant description will give the final answer to all questions regarding the magnetism in  $\text{Na}_2\text{IrO}_3$ . However, relying solely on the localized picture and, correspondingly, on the nnKH model, is, apparently, inadequate.

## VII. CONCLUSIONS

In summary, we have performed an extensive investigation of the electronic properties of  $\text{Na}_2\text{IrO}_3$  in the framework of non-relativistic and relativistic density functional theory calculations and derived by means of the Wannier function projector method, the corresponding microscopic parameters. We resolved the following open questions: (1) By considering various idealized crystal structures for  $\text{Na}_2\text{IrO}_3$  we could disentangle the effect of each of the structural distortions present in this system and concluded that it is the joint effect of these distortions that constructively enhances the intrahexagon effective hopping parameters and suppresses the interhexagon ones favoring the formation of quasi-molecular orbitals. (2) We modelled the relativistic DFT results in terms of a tight-binding model including the spin-orbit coupling term and analyzed the electronic properties of  $\text{Na}_2\text{IrO}_3$  in terms of two complementary descriptions, the (itinerant) quasi-molecular basis and the (localized) relativistic  $j_{\text{eff}}$  basis. We observed that the behavior of  $\text{Na}_2\text{IrO}_3$  lies in between the fully itinerant and the fully localized description and that a quasi-molecular orbital description keeps its character even at large values of the

spin-orbit coupling strength. (3) We showed that XAS and RIXS observations can be well understood within an itinerant description of  $\text{Na}_2\text{IrO}_3$  in contrast to other iridates like  $\text{Sr}_3\text{CuIrO}_6$  where localization is imposed by the crystallographic arrangement of the  $\text{IrO}_6$  octahedra<sup>40</sup>. (4) Finally, we provided *ab initio*-derived estimates for the parameters appearing in the Kitaev and Heisenberg terms in  $\text{Na}_2\text{IrO}_3$  and found that the recently proposed nnKH model (see Section VI), even though it is a very interesting model *per se*, is unfortunately not realistic for  $\text{Na}_2\text{IrO}_3$ . In conclusion, in order to obtain a full understanding of the behavior of  $\text{Na}_2\text{IrO}_3$  all three features; spin-orbit, Coulomb correlations and delocalization of valence electrons over  $\text{Ir}_6$  hexagons are essential.

H.O.J., D.Kh. and R.V. acknowledge support by the Deutsche Forschungsgemeinschaft through grants SFB/TR 49 and FOR 1346 (H.O.J. and R.V.) and SFB 608 and FOR 1346 (D.Kh.).

## VIII. APPENDIX. IDEALIZED $\text{Na}_2\text{IrO}_3$ CRYSTAL STRUCTURES AS USED IN WIEN2k

### A. Experimental structure from Ref. 8

| Space group $C2/m$ (No. 12)  |        |        |        |
|--|--------|--------|--------|
| $a = 5.4269 \text{ \AA}$ , $b = 6.4104 \text{ \AA}$ , $c = 9.3949 \text{ \AA}$ , $\gamma = 124.12^\circ$ |        |        |        |
| Atom   | $x$    | $y$    | $z$    |
| Na1  | 0.0    | 0.0    | 0.5    |
| Na2  | 0.5    | 0.5    | 0.0    |
| Na3  | 0.5    | 0.5    | 0.3400 |
| Ir   | 0.0    | 0.0    | 0.1670 |
| O1   | 0.4590 | 0.2110 | 0.1780 |
| O2   | 0.0070 | 0.7960 | 0.0    |

### B. Idealized structure $S_1$

| Space group $C2/m$ (No. 12)  |        |        |        |
|--|--------|--------|--------|
| $a = 5.4501 \text{ \AA}$ , $b = 6.4411 \text{ \AA}$ , $c = 9.4399 \text{ \AA}$ , $\gamma = 125.26^\circ$ |        |        |        |
| Atom   | $x$    | $y$    | $z$    |
| Na1  | 0.0    | 0.0    | 0.5    |
| Na2  | 0.5    | 0.5    | 0.0    |
| Na3  | 0.5    | 0.5    | 0.3333 |
| Ir   | 0.0    | 0.0    | 0.1667 |
| O1   | 0.4646 | 0.2097 | 0.1785 |
| O2   | 0.0000 | 0.7903 | 0.0    |

### C. Idealized structure $S_2$

| Space group $C2/m$ (No. 12)  |        |        |        |
|--|--------|--------|--------|
| $a = 5.4501 \text{ \AA}$ , $b = 6.4190 \text{ \AA}$ , $c = 9.4399 \text{ \AA}$ , $\gamma = 124.47^\circ$ |        |        |        |
| Atom   | $x$    | $y$    | $z$    |
| Na1  | 0.0    | 0.0    | 0.5    |
| Na2  | 0.5    | 0.5    | 0.0    |
| Na3  | 0.5    | 0.5    | 0.3333 |
| Ir   | 0.0    | 0.0    | 0.1667 |
| O1   | 0.4606 | 0.1909 | 0.1667 |
| O2   | 0.0000 | 0.8091 | 0.0    |

### D. Idealized structure $S_3$

| Space group $C2/m$ (No. 12)  |        |        |        |
|--|--------|--------|--------|
| $a = 5.0658 \text{ \AA}$ , $b = 5.9869 \text{ \AA}$ , $c = 8.7743 \text{ \AA}$ , $\gamma = 125.26^\circ$ |        |        |        |
| Atom   | $x$    | $y$    | $z$    |
| Na1  | 0.0    | 0.0    | 0.5    |
| Na2  | 0.5    | 0.5    | 0.0    |
| Na3  | 0.5    | 0.5    | 0.3333 |
| Ir   | 0.0    | 0.0    | 0.1667 |
| O1   | 0.5000 | 0.2443 | 0.1667 |
| O2   | 0.0000 | 0.7557 | 0.0    |

Note that due to the necessity of using a monoclinic angle  $\gamma$  in WIEN2k, the Ir honeycomb layers in the  $\text{Na}_2\text{IrO}_3$  unit cells presented above are parallel to the  $ac$  plane. Accordingly, within this convention the vector of the Bloch factors in Eqs. (4) and (7) is given by

$$T_{M=1\dots 6}(\mathbf{k}) = (1, e^{-ik_x\tilde{a}}, e^{ik_z\tilde{c}}, e^{i(k_z\tilde{c}-k_x\tilde{a})}, e^{ik_z\tilde{c}}, e^{-ik_x\tilde{a}}), \quad (18)$$

where  $\tilde{a}$  and  $\tilde{c}$  are the lengths of the two primitive lattice vectors lying in the  $ac$  plane. Here, one explicitly accounts for the choice of WIEN2k of the actual positions of the two Ir atoms in the primitive unit cell, which are, *e. g.*,  $(-0.167, 0, 0.167)$  and  $(-0.833, 0, 0.833)$  in the experimental  $\text{Na}_2\text{IrO}_3$  structure.

<sup>1</sup> B. J. Kim, H. Ohsum, T. Komesu, S. Sakai, T. Morita, H. Takagi, T. Arima, Science **323**, 1329 (2009).

<sup>2</sup> J. Chaloupka, G. Jackeli, and G. Khaliullin, Phys. Rev. Lett. **105**, 027204 (2010).

<sup>3</sup> J. Reuther, R. Thomale, and S. Trebst, Phys. Rev. B **84**, 100406(R) (2011).

<sup>4</sup> J. Chaloupka, G. Jackeli, and G. Khaliullin, Phys. Rev. Lett. **110**, 097204 (2013).

- <sup>5</sup> I. I. Mazin, H. O. Jeschke, K. Foyevtsova, R. Valentí, and D. I. Khomskii, Phys. Rev. Lett. **109**, 197201 (2012). Please note that the corresponding  $B_{1u}$  eigenenergy in Table I of this publication should read  $-2(t'_1 - t'_2)$  and the upper two levels merge at  $|t'_1/t'_2| = 3$ . Note that  $t'_1$  and  $t'_2$  are labeled  $t_{1\text{O}}$  and  $t_{2\text{O}}$  respectively in the present work.
- <sup>6</sup> The spin-orbit splitting is given by the difference of the eigenvalues  $\lambda/2$  and  $-\lambda$  in the  $j_{\text{eff}}$  space.
- <sup>7</sup> Y. Singh, S. Manni, J. Reuther, T. Berlijn, R. Thomale, W. Ku, S. Trebst, P. Gegenwart, Phys. Rev. Lett. **108**, 127203 (2012).
- <sup>8</sup> S. K. Choi, R. Coldea, A. N. Kolmogorov, T. Lancaster, I. I. Mazin, S. J. Blundell, P. G. Radaelli, Y. Singh, P. Gegenwart, K. R. Choi, S.-W. Cheong, P. J. Baker, C. Stock, and J. Taylor, Phys. Rev. Lett. **108**, 127204 (2012).
- <sup>9</sup> From these considerations, one can think of other materials with basically the same structure, in which 1/3 of the in-plane *foreign* atoms  $M$  in  $\text{Na}(M_{1/3}\text{Ir}_{2/3})\text{O}_2$  can be any metal  $M$ . Such a program was recently realized by the group of R. J. Cava (private communication).
- <sup>10</sup> Y. Singh and P. Gegenwart, Phys. Rev. B **82**, 064412 (2010).
- <sup>11</sup> R. Comin, G. Levy, B. Ludbrook, Z.-H. Zhu, C. N. Veenstra, J. A. Rosen, Y. Singh, P. Gegenwart, D. Stricker, J. N. Hancock, D. van der Marel, I. S. Elfimov, A. Damascelli, Phys. Rev. Lett. **109**, 266406 (2012).
- <sup>12</sup> P. Blaha, K. Schwarz, G. K. H. Madsen, D. Kvasnicka, and J. Luitz 2001 WIEN2k, *An Augmented PlaneWave+LocalOrbitals Program for Calculating Crystal Properties* (Karlheinz Schwarz, Techn. Universität Wien, Austria).
- <sup>13</sup> J. P. Perdew, K. Burke and M. Ernzerhof, Phys. Rev. Lett. **77** 3865 (1996).
- <sup>14</sup> S. Cottenier, *Density Functional Theory and the family of (L)APW-methods: a step-by-step introduction* (Instituut voor Kern- en Stralingsfysica, K.U.Leuven, Belgium), 2002, ISBN 90-807215-1-4 (to be found at [http://www.wien2k.at/reg\\_user/textbooks](http://www.wien2k.at/reg_user/textbooks)).
- <sup>15</sup> M. Aichhorn, L. Pourovskii, V. Vildosola, M. Ferrero, O. Parcollet, T. Miyake, A. Georges, S. Biermann, Phys. Rev. B, **80**, 085101 (2009).
- <sup>16</sup> J. Ferber, K. Foyevtsova, H. O. Jeschke, R. Valentí, arXiv:1209.4466 (unpublished).
- <sup>17</sup> The description of the orbital character in the present work is done according to the local cubic coordinate system if not explicitly specified otherwise.
- <sup>18</sup> K. Koepnick and H. Eschrig, Phys. Rev. B **59**, 1743 (1999); <http://www.FPLO.de>
- <sup>19</sup> In Fig. 6 we visualize real-valued combinations of degenerate  $E_{2u}$  or  $E_{1g}$  QMOs.
- <sup>20</sup> We compared our prepared idealized structures to those provided by Radu Coldea (private communication) and the agreement between both sets of structures is very good.
- <sup>21</sup> C. Martins, M. Aichhorn, L. Vaugier, S. Biermann, Phys. Rev. Lett. **107**, 266404 (2011).
- <sup>22</sup> A. Shitade, H. Katsura, J. Kuneš, X.-L. Qi, S.-C. Zhang, and N. Nagaosa, Phys. Rev. Lett. **102**, 256403 (2009).
- <sup>23</sup> Note that these states are eigenstates of Eq. (6) after diagonalizing the matrix Eq. (6) and performing an appropriate rotation.
- <sup>24</sup> Orthorhombic distortion lifts the degeneracy of the  $E_{1g}$  and  $E_{2u}$  states combining them into real functions.
- <sup>25</sup> In the ideal case, one would have, *e. g.*,  $B_{1u} \uparrow = (-0.408, -0.408, -0.408, 0.408, 0.408, 0.408, 0, 0, 0, 0, 0)$ .
- <sup>26</sup> D. Haskel, G. Fabbri, M. Zhernenkov, P. P. Kong, C. Q. Jin, G. Cao, and M. van Veenendaal, Phys. Rev. Lett. **109**, 027204 (2012).
- <sup>27</sup> L. C. Chapon and S. W. Lovesey, J. Phys.: Condens. Matter **23**, 252201 (2011).
- <sup>28</sup> S. W. Lovesey and A. N. Dobrynin, J. Phys.: Condens. Matter **24**, 382201 (2012).
- <sup>29</sup> S. W. Lovesey, D. D. Khalyavin, P. Manuel, L. C. Chapon, G. Cao and T. F. Qi, J. Phys.: Condens. Matter **24**, 496003 (2012).
- <sup>30</sup> G. van der Laan and B. T. Thole, Phys. Rev. Lett. **60**, 1977 (1988).
- <sup>31</sup> B. T. Thole, and G. van der Laan, Phys. Rev. B **38** 3158 (1988).
- <sup>32</sup> J. P. Clancy, N. Chen, C. Y. Kim, W. F. Chen, K. W. Plumb, B. C. Jeon, T. W. Noh, and Y.-J. Kim, Phys. Rev. B **86**, 195131 (2012).
- <sup>33</sup> H. Gretarsson, J. P. Clancy, X. Liu, J. P. Hill, E. Bozin, Y. Singh, S. Manni, P. Gegenwart, J. Kim, A. H. Said, D. Casa, T. Gog, M. H. Upton, H.-S. Kim, J. Yu, V. M. Katukuri, L. Hozoi, J. van den Brink, and Y.-J. Kim, Phys. Rev. Lett. **110**, 076402 (2013).
- <sup>34</sup> Y. Yu, L. Liang, Q. Niu, S. Qin, **87**, 041107(R) (2013).
- <sup>35</sup> G. Khaliullin, private communication.
- <sup>36</sup> I. I. Mazin and D. J. Singh, Phys. Rev. B **56**, 2556 (1997).
- <sup>37</sup> A. G. Petukhov, I. I. Mazin, L. Chioncel and A. I. Lichtenstein, Phys. Rev. B **67**, 153106 (2003).
- <sup>38</sup> H. Ishida, M. D. Johannes, and A. Liebsch, Phys. Rev. Lett. **94**, 196401 (2005).
- <sup>39</sup> See for instance, M. Aichhorn, L. Pourovskii, and A. Georges, Phys. Rev. B **84**, 054529 (2011).
- <sup>40</sup> X. Liu, Vamshi M. Katukuri, L. Hozoi, W.-G. Yin, M. P. M. Dean, M. H. Upton, J. Kim, D. Casa, A. Said, T. Gog, T. F. Qi, G. Cao, A. M. Tsvelik, J. van den Brink, and J. P. Hill, Phys. Rev. Lett. **109**, 157401 (2012).